ARPIN DEFICIENCY INCREASES ACTOMYOSIN CONTRACTILITY AND VASCULAR PERMEABILITY

Armando Montoya-García[1], Idaira M. Guerrero-Fonseca[1], Sandra D. Chánez-Paredes[1,§], Karina B. Hernández-Almaraz[1], Iliana I. León-Vega[1], Angélica Silva-Olivares[2], Abigail Bentazos[2], Mónica Mondragón-Castelán[3], Ricardo Mondragón-Flores[3], Citlaltepetl Salinas-Lara[4], Hilda Vargas-Robles[1], and Michael Schnoor[1,*].

[1]Department of Molecular Biomedicine CINVESTAV-IPN, IPN Avenue 2508, 07360 Mexico City, Mexico.

[2]Department of Infectomics and Molecular Pathogenesis CINVESTAV-IPN, IPN Avenue 2508, 07360 Mexico City, Mexico.

[3]Department of Biochemistry, CINVESTAV-IPN, IPN Avenue 2508, 07360 Mexico City, Mexico.

[4]Laboratorio de Patogénesis Molecular, Facultad de Estudios Superiores de Iztacala, UNAM, 54090 Tlalnepantla de Baz, Mexico.

[§]Current address: Laboratory of Mucosal Barrier Pathobiology, Department of Pathology, Brigham and Women's Hospital, Harvard Medical School, 02115 Boston Chestnut Hill, MA, USA.

[*]Correspondence to: Michael Schnoor (mschnoor@cinvestav.mx)

Running title: Arpin controls endothelial barrier integrity

Preprint version: https://www.biorxiv.org/content/10.1101/2023.05.29.542762v1

doi: https://doi.org/10.1101/2023.05.29.542762

ABBREVIATIONS

ABP: Actin-binding protein

Arp2/3: Actin related protein 2/3 complex

EC: Endothelial cells

HMEC-1: Human microvascular endothelial cell line-1

HUVEC: Human umbilical vein endothelial cells

MLC: Myosin Light Chain

MYPT1: Myosin Phosphatase Target Subunit 1

ROCK: Rho-associated protein kinase

WAVE: WASP family Verprolin homolog

ZIPK: Zipper interacting protein kinase

SUMMARY

The expression and functions of arpin in endothelial cells are unknown. We show that arpin controls actomyosin contractility and endothelial barrier integrity in an Arp2/3-independent manner via ROCK1/ZIPK. Arpin-deficient mice are viable, but also show increased basal and induced vascular permeability.

ABSTRACT

Arpin was discovered as an inhibitor of the Arp2/3 complex localized at the lamellipodial tip of fibroblasts, where it regulated migration steering. Recently, we showed that arpin stabilizes the epithelial barrier in an Arp2/3-dependent manner. However, expression and functions of arpin in endothelial cells (EC) have not yet been described. Arpin mRNA and protein are expressed in EC and downregulated by pro-inflammatory cytokines. Arpin depletion in HUVEC causes the formation of actomyosin stress fibers leading to increased permeability in an Arp2/3-independent manner. Instead, inhibitors of ROCK1 and ZIPK, kinases involved in the generation of stress fibers, normalize the loss-of-arpin effects on actin filaments and permeability. Arpin-deficient mice are viable but show a characteristic vascular phenotype in the lung including edema, microhemorrhage and vascular congestion, increased F-actin levels and vascular permeability. Our data show that, apart from being an Arp2/3 inhibitor, arpin is also a regulator of actomyosin contractility and endothelial barrier integrity.

INTRODUCTION

Arpin was discovered ten years ago in fibroblasts as a protein that binds to and inhibits the heptameric actin nucleator actin-related protein 2/3 (Arp2/3) complex (Dang et al. 2013). Arpin competed with WAVE2, a nucleation promoting factor (NPF) that activates Arp2/3, at the lamellipodial tip of migrating fibroblast to steer random migration by regulating migration speed and directional persistence (Dang et al. 2013). However, later studies demonstrated that arpin did not regulate chemotaxis (Dang et al. 2017). Subsequently, arpin has been studied in different cancer types (Lomakina et al. 2016; Li, Zheng, et al. 2017; Zhang, Li, et al. 2019), where its downregulation correlated with poor prognosis of the disease and high migratory capability and invasiveness of the tumor cells (Li, Qiu, et al. 2017; Lomakina et al. 2016). We have shown that arpin was expressed in colon epithelial cells and that patients with ulcerative colitis had lower levels of arpin in acutely inflamed tissue areas. Arpin colocalized with junctional proteins and stabilized epithelial barrier integrity under basal and inflammatory conditions in an Arp2/3-dependent manner (Chanez-Paredes et al. 2021). However, nothing is known about arpin expression in endothelial cells (EC) and functions in endothelial barrier regulation during inflammation.

The endothelium forms a semi-permeable barrier that separates the blood from tissues. During inflammation, weakening of cell-cell adhesive structures including adherens junctions (AJ) and tight junctions (TJ) is important for allowing the passage of plasma proteins and immune cells to the inflamed tissue and inflammation resolution (Reglero-Real et al. 2016). The correct regulation of AJ and

TJ stability and thus vascular permeability is controlled by dynamic actin cytoskeletal remodeling including the formation of stabilizing cortical actin filaments and destabilizing contractile stress fibers (Prasain and Stevens 2009; Garcia-Ponce et al. 2015). As important actin cytoskeletal regulator, the Arp2/3 complex regulates maintenance and recovery of the pulmonary endothelial barrier (Belvitch et al. 2017). On the other hand, Arp2/3 is also involved in the endocytosis of occludin at the blood-brain barrier during inflammation (Park et al. 2013). Additionally, Arp2/3 and its activator WAVE-2 stabilize endothelial barrier functions by promoting the formation of junction-associated intermittent lamellipodia (JAIL) (Abu Taha et al. 2014). These studies are only a few examples highlighting the importance of the Arp2/3 complex for controlling vascular permeability. While Arp2/3 activators such as WAVE-2 have been studied in this context, the role of Arp2/3 inhibitors in endothelial barrier regulation remains elusive. Therefore, we hypothesized that arpin is expressed in endothelial cells and that it contributes to the regulation of actin cytoskeleton dynamics at junctions to fine-tune the regulation of endothelial permeability under basal and inflammatory conditions. To test this hypothesis, we generated arpin-depleted Human Umbilical Vein Endothelial Cells (HUVEC) and arpin-deficient mice to analyze the role of arpin in endothelial barrier regulation *in vitro* and *in vivo*.

RESULTS

Arpin is expressed in endothelial cells.

Arpin was discovered in fibroblasts (Dang et al. 2013), and it was subsequently described to be expressed in other cells including colon epithelial cells (Chanez-Paredes et al. 2021). However, it remains unknown whether arpin is expressed in endothelial cells. We found here by end-point RT-PCR that arpin mRNA is expressed in different human and mouse endothelial cells (Figure 1A). Also, arpin protein is present in HMEC-1 and HUVEC at similar levels with the predicted molecular weight of 25 kDa (Figure 1B).

Arpin was localized throughout the cytosol in confluent HUVEC monolayers (Figure 1C). However, line scans revealed an enrichment of arpin close to vascular endothelial cadherin (VE-cadherin) at cell-cell contacts. (Figure 1C). Analyzing arpin localization in postcapillary venules of cremaster muscles using PECAM-1 as template for endothelial cell-cell contacts, we observed a similar localization of arpin throughout the endothelial cytosol with an enrichment near and at junctions (Figure 1D). Although the majority of arpin is localized in the cytosol, such enrichment at junctions observed both in human HUVEC culture and mouse cremaster venules suggests that arpin could contribute to endothelial barrier regulation.

Arpin is dowregulated by inflammatory cytokines.

Endothelial cells are activated by pro-inflammatory cytokines such as TNFα and IL-1β leading to weakening of the endothelial barrier (Chen et al. 2021; Mako et al. 2010). To study arpin regulation during inflammation, we analyzed *ARPIN* gene expression by qRT-PCR in HUVEC monolayers treated with TNFα for 4 and 18 h and found a significant downregulation of around 60% (Figure 2A). Remarkably, expression of the other Arp2/3 inhibitors, *AP1AR* and *PICK1*, was not significantly changed after TNFα treatment. Western blot and densitometry analysis confirmed the decrease of arpin at the protein level (Figure 2B) with no significant changes of PICK1 protein levels (Figure S1A). Upregulation of Intercellular Adhesion Molecule-1 (ICAM-1) was used here as a positive control for the inflammatory response.

Immunofluorescence of arpin in HUVEC monolayers treated or not with TNFα confirmed downregulation of arpin (Figure 2C). This decrease was not only obvious for total arpin, but arpin was also lost at junctions (arrows in the magnifications of Figure 2C) and actin filaments (Top-right graphs Figure 2C). Interestingly, arpin reduction significantly correlated with the TNFα-induced increase in actin stress fibers (lower graph Figure 2C) (Wojciak-Stothard et al. 1998). Arpin protein downregulation was also observed after IL-1β treatment in HUVECs for 4 and 18 h (Figure S1B) and no significant changes were observed in the protein levels of PICK1 (Figure S1C). Similar with TNFα-treatment, IL-1β induces loss of arpin at all subcellular locations (Top-right graphs Figure S1D). Again, IL1β-induced arpin downregulation significantly correlated with an increase in actin stress fibers (lower graph Figure S1D).

Arpin immunofluorescence signal in post-capillary venules of the TNFα-inflamed cremaster muscle was also reduced by around 50%, which was again true for both junctional and non-junctional arpin (Figure 2D). Robust neutrophil recruitment confirmed that inflammation was induced correctly in this model. Overall, endothelial arpin is downregulated in response to pro-inflammatory cytokines *in vitro* and *in vivo* suggesting that arpin plays an important role in the regulation of endothelial barrier dysfunction during inflammation.

Arpin depletion increases endothelial permeability and modifies junction architecture.

To analyze the function of arpin in endothelial barrier regulation, we generated arpin-depleted HUVEC with more than 80% reduction in arpin protein levels (Figure 3A). Of note, arpin depletion did not change the expression of arpC5, a subunit of the Arp2/3 complex, or the NPFs WAVE2 and WASP (Figure 3A). Although arpin-depleted HUVEC formed monolayers, the paracellular flux of 150 kDa FITC-dextran across untreated arpin-depleted HUVEC monolayers was 34.5% (±3.70) higher (Figure 3B). While TNFα treatment of control HUVEC induced the expected strong increase in permeability, TNFα treatment of arpin-depleted HUVEC showed an even higher increase compared to control HUVEC treated with TNFα (Figure 3B) suggesting that the TNFα-induced and arpin-induced permeability increases are regulated by different mechanisms. However, we did not observe changes in the total protein levels of the AJ proteins VE-Cadherin, β-catenin, and vinculin in control and arpin-depleted HUVEC (Figure 3C), or in the

levels of the TJ proteins ZO-1 and claudin-5 (Figure 3D). However, immunofluorescence staining of VE-Cadherin and β-catenin revealed discontinuous and zipper-like junctional patterns, indicative of immature junctions in arpin-depleted HUVEC (Figure 3E). Surprisingly, calcium switch assay showed that control and arpin-depleted HUVEC formed new junctions in a similar fashion (Figure S2A). These data suggest that arpin is not required for junction assembly, but rather for stabilizing existing junctions.

Arpin depletion induces actin filament formation.

It is well known that the endothelial actin cytoskeleton contributes to barrier homeostasis and that significant actin cytoskeleton remodelling accompanies increased vascular permeability (Garcia Ponce et al. 2016; Hilfenhaus et al. 2018; Waschke et al. 2005). Thus, we analyzed F-actin using phalloidin staining in control and arpin-depleted HUVEC. Quantifying the pixel intensity of the phalloidin stainings, we observed a statistically significant increase in actin filaments in the cells with arpin deficiency (Figure 4A). Particularly, arpin-depleted HUVEC showed a significant increase in central actin filaments crossing the cell body (Figure 4B). However, we did not observe significant differences in the total actin protein levels in control and arpin-depleted HUVEC (Figure 4C) suggesting that G-actin levels are reduced at the expense of F-actin formation. Quantification of other proteins known to be involved in actin dynamics such as cortactin, coronin1B, and cofilin did not reveal any significant changes caused by the loss of arpin (Figure 4D). In the next set of experiments, we wanted to identify the nature of these actin filaments

and answer the question of whether the observed hyperpermeability is related to these changes in the actin cytoskeleton.

Inhibition of the Arp2/3 complex does not rescue the observed phenotype in arpin-depleted HUVEC.

The first function of arpin described was that it inhibits the Arp2/3 complex (Dang et al. 2013). Assuming this function, loss of arpin would mean more active Arp2/3. To determine if a potential increase in Arp2/3 activity is causing the observed effects in arpin-depleted endothelial cells, we used the pharmacological Arp2/3 inhibitor CK666 to test whether it would reverse the observed phenotype (Figure 5). Surprisingly, phalloidin stainings and quantification of the total F-actin signal revealed no reduction in the pixel intensity between CK666-treated and vehicle-treated arpin-depleted HUVEC (Figure 5 A and B). The central actin fiber density was also not affected by Arp2/3 inhibition in arpin-depleted HUVEC (Figure 5C). Interestingly, permeability increased in control HUVEC after CK666 treatment (Figure 5D). Instead of normalizing the permeability in arpin-depleted HUVEC, CK666 induced an additional increase in permeability (Figure 5D). These surprising results demonstrate that arpin regulates actin filament formation and permeability in HUVEC in an Arp2/3-independent manner.

Arpin depletion leads to increased formation of actin stress fibers.

Given that arpin acts independently of the Arp2/3 complex in HUVEC and that the observed central actin filaments in arpin-depleted HUVECs resemble stress fibers (Tojkander, Gateva, and Lappalainen 2012), we investigated whether these actin structures are contractile actomyosin stress fibers, which are known to exert mechanical forces on junctions and thus destabilize endothelial contacts (Millan et al. 2010). As shown in Figure 6A, we observed a significant increase in the phosphorylation of myosin light chain (MLC) at serine-19 in arpin-depleted HUVECs, indicative of actomyosin contractility. MLC is a target of kinases such as ROCK1 and ZIPK that phosphorylate it, and phosphatases such as Myosin Phosphatase Target Subunit 1 (MYPT1) that dephosphorylate MLC. Concomitant with the increase in p-MLC-S19, we found an increase in the phosphorylation of MYPT1 at Threonin-696 and Threonin-853 in arpin-depleted HUVECs (Figure 6B), phosphorylations known to inactivate MYPT1. In agreement, we observed increased total levels of ROCK1 and ZIPK in arpin-depleted HUVECs that likely contribute to increased MLC phosphorylation (Figure 6C). However, the levels of the formin mDia, implicated in the nucleation of actin stress fibers, were not affected by arpin depletion (Figure 6C). These results suggest that the increased central actin filaments in arpin-depleted HUVEC are contractile actomyosin stress fibers that contribute to the destabilization of endothelial junctions and increased permeability.

Inhibition of ROCK1/2M and ZIPK rescues endothelial barrier functions in arpin-depleted HUVEC.

Given the increased levels of ROCK1 and ZIPK and the increased phosphorylation of MLC and MYPT1, we hypothesized that pharmacological inhibition of ROCK1 by Y27632 and of ZIPK by HS38 could revert increased stress fiber formation and permeability in arpin-depleted HUVEC. Phalloidin staining in arpin-depleted HUVECs treated with Y27632 (Figure 7A) showed indeed a reduction of the total levels of actin filaments (Figure 7B) and the central actin fiber density (Figure 7C) when compared to vehicle-treated arpin-depleted HUVEC. However, it was not reduced to the levels seen in Y27632-treated control HUVEC that were significantly lower compared to vehicle-treated control cells. Similar results were observed in permeability assays (Figure 7D). While the permeability in Y27632-treated arpin-depleted HUVEC were reduced to the levels of vehicle-treated control HUVEC, they were still higher compared to Y27632-treated control HUVEC.

Moreover, we observed that arpin-depleted HUVECs treated with the ZIPK inhibitor HS38 showed total actin levels (Figure 7E and 7F) and central actin fiber density (Figure 7G) similar to control HUVEC treated with HS38 or vehicle. In contrast to Y27632, HS38 was not able to reduce actin filament formation in control HUVEC. Permeability assays confirmed these data and showed a complete rescue in arpin-depleted HUVEC treated with HS38 (Figure 7H). Of note, the even higher permeability in TNFα-treated arpin-depleted HUVECs was reduced after HS38 treatment but not to the levels of control cells indicating that ZIPK inhibition is able to rescue the permeability effect caused by the loss of arpin, but not the combined effect of TNFα treatment and loss of arpin (Figure 7I). This result further suggests

that TNFα-induced permeability follows a different mechanism than the permeability effect caused by arpin depletion.

Generation and characterization of arpin-deficient mice.

Finally, to unravel the role or arpin in vascular permeability, we generated an arpin knockout mouse model on the C57BL/6 genetic background using CRISPR/Cas9-mediated genome engineering targeting exon 3 with a pair of specific gRNA sequences (Figure 8A). PCR of genomic DNA samples extracted from the tails clearly distinguishes the 3 genotypes (Figure 8B); and Western blot of arpin revealed its presence in different organs of wild-type mice, and its absence in knock-out mice (Figure 8C). Arpin$^{-/-}$ mice did not show any obvious phenotype and could not be distinguished by visual inspection. We did not observed changes in development, appearance, weight (Figure S3A), or susceptibility to diseases compared to arpin$^{+/+}$ mice in pathogen-free conditions. Breeding female and male arpin$^{+/-}$ mice generated offspring according to Mendelian ratios (Table S1).

Arpin deficiency causes increased vascular permeability.

To unravel whether arpin also regulates endothelial barrier integrity *in vivo*, we performed permeability assays *in vivo* in the lung because WT mice showed high levels of arpin in the lung (Figure 8C) and the lung is a highly vascularized organ. Remarkably, permeability in lungs of arpin$^{-/-}$ mice was around two-fold higher than in arpin$^{+/+}$ mice under basal conditions without any permeability-inducing stimulus (Figure 8D). To rule out that this is an effect specific only for the lung, we also performed Miles assays to measure permeability in the back skin

under basal condition and with histamine as a permeability-inducing stimulus. Also in the skin, vascular permeability was higher in arpin$^{-/-}$ mice under basal conditions compared to arpin$^{+/+}$ mice (Figure 8E). Of note, histamine stimulation further induced permeability in arpin$^{-/-}$ mice. Treatment with either the ROCK1/2 inhibitor Y27632 or the ZIPK inhibitor HS38 reverted permeability to the basal levels observed in arpin$^{+/+}$ mice, thus confirming our findings in arpin-depleted HUVEC. Interestingly, Arp2/3 inhibition using CK-666 did not affect vascular permeability in the skin of arpin$^{-/-}$ mice (Figure 8E). Together, these results support the idea that arpin controls endothelial permeability via ROCK/ZIPK-dependent stress fiber formation and not via inhibition of the Arp2/3 complex. Next, we analyzed the protein levels of different junction proteins by Western blot and did not observe any significant differences in the protein levels of VE-Cadherin, β-catenin, vinculin, claudin-1 and -5, and tubulin in arpin$^{+/+}$ and arpin$^{-/-}$ lungs (Figure S3B).

Histological analyses revealed normal lung histology in arpin$^{+/+}$ mice (Figure 8F, images 1 and 2). By contrast, the arpin$^{-/-}$ lungs showed several abnormalities indicative of a vascular phenotype. For example, absence of arpin caused a reduction of the volume of the alveolar space (Figure 8F, image 3, asterisk), signs of hemorrhage and microhemorrhage (Figure 8F, images 4 and 5, arrowheads), and presence of interalveolar edema (Figure 8F, image 6, asterisks). Accordingly, the histological score was significantly increased in arpin$^{-/-}$ mice (Figure 8F, graph below). Lungs of arpin$^{-/-}$ mice also showed the presence of lymphocytes and macrophages. However, hemograms revealed that the number of leukocytes in the peripheral blood was not significantly altered in arpin$^{-/-}$ mice compared with arpin$^{+/+}$

mice (Table S2), indicating that the presence of lymphocytes and macrophages in the lungs of arpin$^{-/-}$ mice is not simply due to an increased number of these cells.

PECAM-1 immunostaining was performed to visualize blood vessels in the lung, and phalloidin to identify F-actin (Figure 8G). Although we did not observe differences in total levels of PECAM-1 in arpin$^{+/+}$ and arpin$^{-/-}$ lungs, we observed a significant increase in the total levels of F-actin (Figure 8G, graph below), similar to what we observed in arpin-depleted HUVEC suggesting that the increased permeability *in vivo* is also due to an increase in the formation of actin stress fibers. In addition, we also analyzed endothelial junctions in post-capillary venules of cremaster muscles under basal conditions. We observed in venules of arpin$^{-/-}$ mice VE-Cadherin internalization leading to a zipper-like junction structure similar to what we observed in arpin-depleted HUVEC (Figure S3C). Also, ZO-1 staining showed gaps in arpin$^{-/-}$ mice, whereas it was continuous in arpin$^{+/+}$ mice (Figure S3D). Overall, our data highlight a novel important Arp2/3-independent role of arpin in maintaining endothelial barrier integrity *in vitro and in vivo*.

DISCUSSION

In this study, we discovered new and surprising arpin functions. First, arpin is expressed in endothelium *in vitro* and *in vivo* and downregulated during inflammation. Second, arpin is required for proper endothelial permeability regulation and junction architecture. Third, and most surprisingly, arpin exerts these functions in an Arp2/3-independent manner; instead, it rather controls actomyosin contractility in a ROCK1/ZIPK-dependent mechanism (Figure 9). Finally, we present the first total arpin knock-out mice that are viable and breed and develop normally but show histological characteristics of a vascular phenotype in the lung and increased permeability similar to what we observed in arpin-depleted HUVEC.

Arpin is expressed in EC with a localization throughout the cytosol but with an enrichment at cell-cell contacts similar to what has been described in epithelial cells of the colon, other barrier-forming cells (Abu Taha et al.). Such ubiquitous but diffuse subcellular location in (endothelial) cells is not surprising for an actin-

regulating protein as it has been also described for other actin cytoskeleton regulators such as WAVE2 (Mooren et al. 2014) and the Arp2/3 complex (Abu Taha et al. 2014). The enrichment at junctions, however, suggested that arpin plays a role in the regulation of endothelial barrier integrity. In fibroblasts, arpin was enriched at the lamellipodial tip and accordingly regulated migration speed and directionality, one of the main functions thus far described for arpin. It will be important to reveal in future studies whether arpin also regulates endothelial cell movement for example during angiogenesis.

Of note, arpin is downregulated by pro-inflammatory cytokines suggesting that the removal of arpin is required for the changes in EC occurring during inflammation including actin cytoskeleton remodelling and junction weakening that allow for inflammation-related vascular events such as plasma protein leakage and leukocyte recruitment essential for combating the cause of inflammation and inflammation resolution. This finding is in line with our previous report showing downregulation during epithelial inflammation. Particularly, we demonstrated that arpin is not only reduced in colon epithelial cells after treatment with pro-inflammatory cytokines, but also in a DSS-induced colitis mouse model and in patients with ulcerative colitis, where loss of arpin was particularly evident in acutely inflamed tissue regions. Importantly, loss of arpin significantly correlated with epithelial barrier disruption in all models (Chanez-Paredes et al. 2021) indicating that loss of arpin in the context of epithelium is related to pathogenic events. This is in contrast to our new findings in endothelium where barrier weakening is required for proper inflammation resolution. However, the recovery of

arpin expression during inflammation resolution and the role of arpin in vascular diseases remain to be investigated. Besides, in macrophages infected with human rhinovirus arpin was also reduced leading to impaired phagocytosis (Jubrail et al. 2020). Thus, arpin downregulation seems to be relevant in different cell types to regulate different cellular functions. Our qRT-PCR results suggest that arpin reduction occurs at the transcriptional level. However, more research is needed to characterize the promoter region of arpin and regulatory mechanisms controlling arpin mRNA levels. Given the strong downregulation induced by cytokines such as TNFα it is tempting to speculate that arpin mRNA levels are controlled by inflammatory pathways that are well known to be induced by TNFα such as NF-κB.

The Arp2/3 complex is critical for endothelial barrier formation, maintenance and recovery (Abu Taha et al. 2014; Belvitch et al. 2017). Therefore, it was logical to assume that an Arp2/3 inhibitory protein such as arpin would be important for endothelial barrier integrity regulation. This idea was further supported by our study showing that arpin is involved in epithelial barrier regulation in an Arp2/3-dependent manner. Surprisingly, our results in EC suggest that arpin functions independently of the Arp2/3 complex. Instead, we described here that arpin is involved in the formation of actomyosin stress fibers in a ROCK/ZIPK-dependent fashion. It is well known that in EC ROCK1 and ZIPK are activated downstream of several pro-inflammatory mediators including TNFα (Mong and Wang 2009; Zeng et al. 2021) which leads to the phosphorylation of MLC and MYPT1 that together drive stress fiber formation, actomyosin contractility, reduction of the barrier-stabilizing cortical actin ring and barrier dysfunction (Millan et al. 2010; Angulo-

Urarte et al. 2018). Thus, our findings in arpin-depleted HUVEC of increased actomyosin stress fibers may well explain the observed increased permeability. ZIPK is not just activated but also overexpress by TNFα in ECs (Zeng et al. 2021), its depletion and inhibition reduces thrombin-induced MLC phosphorylation and actomyosin contractility (Zhang, Zhang, et al. 2019), which is in line with our observation in arpin-depleted HUVEC. Together, these data indicate a mechanistic link of arpin and ZIPK for EC barrier regulation during inflammation, but more research is required to unravel in detail the exact nature of this link. On the other hand, the spatiotemporal interplay between non-muscle-myosin II-dependent contractility and Arp2/3 complex activity regulates the formation of dactylopodia, a lamellipodia-related membrane protrusion of invasive EC implicated in sprouting angiogenesis (Figueiredo et al. 2021). How such interplay may contribute to inflammatory EC barrier regulation and whether arpin connects the two different actin dynamics mechanisms are questions to be answered by future research.

Loss of the actin-binding protein (ABP) cortactin, which has also been implicated in the regulation of Arp2/3-induced actin branches, has also been shown to cause increased actomyosin contractility and as a consequence increased EC hyperpermeability (Garcia Ponce et al. 2016). It remains elusive why barrier functions in EC and epithelial cells are regulated by arpin via different mechanisms, but this question is the focus of ongoing and future studies.

Although originally not described as an ABP, we do not discard the possibility that arpin can directly regulate actin cytoskeleton remodelling because a recently published actin interactome revealed that actin can interact transiently with

arpin (Viita et al. 2019). Thus, it will be important to unravel whether arpin interacts with G-actin, F-actin, or both; and how this direct interaction would contribute to the regulation of the actin dynamics, junction architecture, and barrier regulation in EC.

In this study, we also report for the first time a total arpin knockout C57BL/6 mouse generated by CRISPR/Cas9-mediated genomic engineering. These mice developed and grew normally as C57BL/6 mice at least until week 12 when the arpin-deficient mice were used for experiments. Also, these mice did not show any phenotype identifiable by visual inspection. Thus, arpin is not essential for embryonic, fetal and early adult development similar to what has been described for other ABP knockout mice including those deficient for PICK1 (Steinberg et al. 2006), gadkin (Schachtner et al. 2015), cortactin (Schnoor et al. 2011), α-actinin3 (MacArthur et al. 2008) and coronin-1A (Punwani et al. 2015). By contrast, mice deficient for the Arp2/3 subunits ArpC4 (van der Kammen et al. 2017) and ArpC3 (Yae et al. 2006) and the NPF WAVE2 (Dahl et al. 2003) and N-WASP (Snapper et al. 2001) are not viable, thus further highlighting the difference between Arp2/3 inhibitors and ABP and the Arp2/3 complex and its activators. Importantly, our permeability and histological data revealed a clear vascular phenotype in the lung and therefore the importance of arpin in maintaining endothelial barrier integrity in the lung *in vivo*, a phenotype that is in line with our observations in arpin-depleted HUVEC. Such a strong vascular phenotype in the lung can be caused by several factors including an increase in the intravascular or interstitial hydrostatic pressure, endothelial injury or disruption of tissue barriers or lymphatic insufficiency (Malek and Soufi 2023). While this phenotype in the arpin$^{-/-}$ mice is notorious, it apparently

does not compromise the life of the mice at least into early adulthood. It will be critical to characterize older mice; and to investigate whether these mice are more susceptible to inflammatory or infectious diseases of the lung that are also characterized by the loss of tissue barrier functions. Moreover, future investigations need to analyze arpin functions in other organs such as heart and brain in which arpin is highly expressed.

In conclusion, our results suggest that arpin, besides being an Arp2/3 inhibitor is a fundamental component of the molecular machinery that controls actomyosin contractility and endothelial barrier integrity. We proposed a model in which arpin is downregulated during inflammation to induce the formation of actomyosin stress fibers and vascular permeability. This study will hopefully pave the way for additional studies on the role of arpin in vascular diseases.

MATERIALS AND METHODS

Antibodies and Reagents

Polyclonal antibodies against arpin were obtained by immunizing rabbits with purified full length human arpin (described below). Antibodies against VE-Cadherin (clone F-8), ICAM-1 (clone 15.2), β-catenin (clone E-5) and species-specific peroxidase-labelled secondary antibodies were form Santa Cruz Biotechnology (Santa Cruz, CA). Antibodies against WASP, WAVE2 (clone DSC8), p-Cofilin (S3) (clone 77G2), cofilin, pMLC (Ser19), MLC, pMYPT1 (Thr696), pMYPT1 (Thr 853), MYPT1, ROCK1 (clone C8F7) and DAPK3/ZIPK were purchased from Cell Signaling Technology (Danvers, MA). Antibodies against claudin-5 (clone 4C3C2), ZO-1, Coronin1B and Alexa-labeled secondary antibodies were from Thermo Fisher Scientific (Waltham, MA). The antibody against vinculin was from Sigma Aldrich (St. Louis, MO). Antibodies against PECAM-1 (clone MEC 13.3) and mDia were obtained from BD Bioscience (Franklin Lakes, NJ). The antibody against MRP14 (Clone 2B10) was purchased from US Biological Life Science (Salem, MA). Antibodies against cortactin (clone 289H10) and arpC5 (Clone 232H3) were

kindly provided by Dr. Klemens Rottner and Dr. Theresia Stradal (Helmholtz Centre for Infection Research, Braunschweig, Germany). The monoclonal antibody against actin was kindly provided by Dr. José Manuel Hernández (Department of Cell Biology, Cinvestav-IPN, Mexico City, Mexico). CK666, Y27632 and ML7 were purchased from Sigma-Aldrich. HS38 was purchased from Tocris Bioscience (Bristol, UK).

Expression and purification of Arpin

The full length human arpin sequence cloned into the pET-32a(+) expression vector was from GenScript (Piscataway, NJ). The Arpin-pET-32a(+) construct was used to transform Rosetta (DE3) *E. coli*. Overexpression of the fusion protein was induced by adding 1 mM isopropyl-D-thiogalactopyranoside (IPTG; Sigma Aldrich; St. Louis, MO) to the transformed cell culture. The fusion protein was purified by Ni-NTA agarose affinity chromatography (Quiagen; Valencia, CA) according to the manufacturer's instructions. Protein concentration was determined by DC Assay (Bio-Rad, Hercules, CA) and purity was analyzed by 12% SDS-PAGE.

Production of polyclonal antibodies against arpin.

One rabbit was immunized with 500 µg of recombinant arpin by subcutaneous injection of an emulsified 1:1 mixture of protein and TiterMax Gold (Sigma Aldrich; St. Louis, MO). Three more immunizations were performed 14, 21 and 35 days after the first immunization by subcutaneous injection of 140 µg of recombinant arpin each. Pre-immune and immune sera were analyzed by ELISA and Western blot. All sera were used for western blots and immunofluorescence stainings.

Cell culture

HUVEC were isolated from discarded human umbilical cords as described (Crampton, Davis, and Hughes 2007), cultured in Endothelial Cell Medium (ScienCell Research Laboratories, Carlsbad, CA) at 37°C in a humid atmosphere containing 5% CO_2. HUVEC were used between passages 1-7. For inflammatory conditions, confluent HUVEC monolayers were treated with 15 ng/ml tumor necrosis factor (TNF)α (Peprotech, Mexico-City, Mexico) or 15 ng/ml interleukin (IL)-1β (Peprotech) for the indicated times. Human microvascular endothelial cells (HMEC-1) were cultured in MCDB-131 medium (Sigma-Aldrich) supplemented with 10% Fetal Bovine Serum (FBS), 1 µg/mL hydrocortisone, 20 µg/mL endothelial cell growth supplement, 10 mM L-glutamine, penicillin and streptomycin (Sigma-Aldrich) at 37°C in a humid atmosphere containing 5% CO_2. The mouse brain endothelial cell line bEnd.3 was cultured in DMEM medium (Sigma-Aldrich) supplemented with 10% FBS, penicillin and streptomycin at 37°C in a humid atmosphere containing 5% CO_2. Murine lung endothelial cells (MLEC) were isolated and cultured as described (Garcia Ponce et al. 2016).

Generation of arpin-depleted HUVEC

Stable arpin-depleted HUVEC were generated by lentiviral transduction using the trans-lentiviral packaging kit (Thermo Fisher Scientific, Waltham, MA) and the pLKO.1 plasmid (Addgene, Cambridge, MA) according to the manufacturer's instructions. HUVEC were transduced in passage 2 and selected using puromycin. The following shRNA sequences were used: shCtrl: CGGAGAAGTGGAGAAGCATAC and shArpin: GGAGAACTGATCGATGTATCT (Dang et al. 2013).

End-point PCR and qRT-PCR

RNA was isolated from HUVEC and HMEC-1 using TRIzol (Invitrogen, Carlsbad, CA) according to the manufacturer's instructions and treated with RNase-free DNase I (Thermo Fisher Scientific). cDNA was synthetized using the RevertAid first strand cDNA synthesis kit (Thermo Fisher Scientific), according to the manufacturer's instructions. End-point PCR was performed using the Platinum PCR Super Mix (Thermo Fisher Scientific) with 0.15 µM of each primer and 100 µg cDNA. PCR conditions were: 95°C for 3 min, followed by 35 cycles of 95°C for 30 s, 55°C for 30 s, 72°C for 30 s, and a final extension at 72°C for 10 min. PCR products were separated on 2% agarose gels by electrophoresis.

qRT-PCRs were carried out in a final volume of 10 µl, containing 5.0 µl Power SYBR Green PCR Master Mix (Applied Biosystems, Foster City, CA), 0.15 µM of each primer and 125 µg cDNA using a StepOne™ Real-Time PCR System (Applied Biosystems). PCR conditions were: 95°C for 10 min, followed by 40 cycles of 95°C for 15, 60°C for 60 s, and the melting curve was generated during the last cycle by heating from 60°C to 95°C in increments of 0.5°C/s. Relative expression was quantified using the $2^{-\Delta\Delta CT}$ method with 7SL as housekeeping gene (Rao et al. 2013). Primer sequences were: *7SL*-Fw: ATCGGGTGTCCGCACTAAGTT, *7SL*-Rv: CAGCACGGGAGTTTTGACCT, *ARPIN*-Fw: GCCCAGAGTCACACAGCTAA, *ARPIN*-Rv: CTTTCTGAAGGGCAAGGAAG, *PICK1*-Fw: ATGATTCAGGAGGTGAAGGG, *PICK1*-Rv: CGGTGCTTGACTTTCTTCAA, *AP1AR*-Fw: GAAATGACGACAGCACATCC, *AP1AR*-Rv: TAAGTGCTGCCCGTAGAATG, *Arpin*-Fw: GCTCTCTGTCAATTCCAGCA, *Arpin*-Rv: CACCAGGAAGGTGAACACAG, *Actb*-Fw: TATCCACCTTCCAGCAGATGT, *Actb*-Rv: AGCTCAGTAACAGTCCGCCTA.

Western blot

Equal amounts of protein lysates from cells or tissues were separated by SDS-PAGE, transferred onto 0.45 µm pore nitrocellulose membranes (Bio-Rad, Hercules, CA), and then blocked with Tris-buffered saline (TBS) containing 0.05% Tween and 5% skim-milk or 5% bovine serum albumin (BSA) for 1 h at RT. Immunoblots were incubated with primary antibodies overnight at 4°C, washed and then incubated with HRP-conjugated secondary antibodies for 1 h at RT. Protein bands were visualized and recorded using a ChemiDoc imaging device (Bio-Rad). Pixel intensities of the bands were quantified using ImageJ software (NIH, Bethesda, MD).

Paracellular flux assay

60,000 HUVECs were seeded on 6.5-mm-diameter 0.4-µm pore transwell filters Corning-Costar, Acton, MA,) coated with 0.8% gelatin and cultivated for 72 h. Then, 50 µg of 150 kDa FITC-dextran (Sigma-Aldrich) were added to the upper chamber with fresh medium in the lower chamber and incubated for 1 h at 37°C. Then, 100 µL medium was taken from the lower chamber and the fluorescence was quantified using a fluorometer. Emission values were normalized to control cells (set to 1).

Calcium-switch assay

HUVEC were cultivated on coverslips coated with 0.8% gelatin until confluent. To generate a calcium-free environment, the cells were cultivated for 2 h in ECM medium in the presence of 2.5 mM EGTA to chelate free calcium. After 2 h, the medium was changed to normal ECM medium with calcium. Cells were cultivated for the indicated times, then fixed and stained for VE-Cadherin as described below.

Immunofluorescence staining and microscopy.

HUVEC were seeded on glass coverslips coated with 0.8% gelatin and cultivated to confluence. HUVEC were fixed with 4% paraformaldehyde (PFA) for 10 min at RT and then permeabilized with 0.1% Triton X-100 in PBS for 10 min at 4°C. Then, samples were blocked for 30 min with 3% BSA in PBS. Incubation with primary antibodies in 3% BSA in PBS was performed overnight at 4°C followed by washing and incubation with phalloidin labelled with Alexa-Flour 488. Biolegend, San Diego, CA) and species-specific fluorescently labeled secondary antibodies for 1 h at RT. Preparations were mounted in Vecta-Shield containing 4'6-diamidino-2-phenylindole (DAPI; Thermo Fisher Scientific).

For lung tissue staining, mice were anesthetized and sacrificed. Then a 1:1 dilution of Tissue-Tek (Fisher Health Care, Waltham, MA) and PBS was injected via the trachea into the lungs, and the trachea was ligated to avoid leakage. The lungs were extracted and embedded in Tissue-Tek. The samples were frozen, cut into 8 µm sections using a cryostat (Leica, Wetzlar, Germany) and collected on glass slides. Subsequently, tissue sections were fixed in absolute ethanol at -20 °C for 30 min and incubated with 0.2% $NaHB_4$ for 5 minutes at RT to reduce autofluorescence. Samples were blocked with 6% BSA in PBS + 0.01% Tween. Incubation with primary antibodies in 6% BSA in PBS was performed overnight at 4°C followed by washing and incubation with phalloidin labelled with Rhodamine (Thermo Fisher Scientific) and species-specific fluorescently labeled secondary antibodies for 1 h at RT. The samples were incubated in 0.1% Sudan Black B diluted in 70% ethanol for 5 min at RT to further reduce autofluorescence. Finally, preparations were washed with water and mounted in Vecta-Shield containing DAPI.

For cremaster tissue staining, mice were anesthetized, sacrificed, and the cremasters collected and fixed in 4% PFA for 45 min at 4°C. Next, the tissues were blocked and permeabilized with 25% FBS, 0.5% Triton X-100 in PBS for 4 h at RT. Incubation with primary antibodies in 10% FBS in PBS was performed overnight at 4°C followed by washing and incubation with species-specific fluorescently labeled secondary antibodies for 2 h at RT. Finally, cremaster tissues were washed with PBS and mounted. All samples were examined using a laser confocal microscope (Leica TCS SP8).

Generation of arpin-deficient mice

The arpin$^{-/-}$ mice on a C57Bl/6 genetic background were generated by CYAGEN (Santa Clara, CA) using the CRISPR/Cas9 technology with two gRNA sequences (gRNA3: CTATGCAGCAGGGTAGCGCCAGG and gRNA4: CGCACAGTGATAGTCGGAGCCGG) that target the exon 3 of the arpin mouse gene (Figure 3A). Cas9 mRNA and gRNA sequences were co-injected into fertilized mouse eggs to generate targeted knockout offspring. F0 founder animals were identified by genotyping and sequencing. Positive founders were bred with WT mice to test germline transmission. Positive F1 animals were shipped and used to establish a colony at the animal facility of Cinvestav-IPN. All animal experiments were approved by the institutional animal care and use committee and the bioethics committee of Cinvestav with protocol number 0227-16.

Genotyping

Genomic DNA was prepared from mouse tails dissolved in 12 mM NaOH and 0.2 mM EDTA and incubated at 98°C for 1 h, followed by addition of 40 mM Tris-HCl

pH 5.5. Genotyping to detect the WT and arpin-targeted alleles were performed in two different PCRs using the following primers: forward GCTGGCAACTTCAATCCTGCCT; and reverse GAGACAAACAAGTCAGTCTAACAGCCTC, producing a PCR fragment of 552 bp derived from the WT allele only; and forward GCTGGCAACTTCAATCCTGCCT; and reverse CAGTGTTCCCAGGGCTTGTCTGA, producing PCR fragments with sizes of 1073 bp (WT allele) and ~420 bp (mutant KO allele) (Figure 3B). PCR was performed in a total volume of 10 µL and PCR conditions were: 94 °C for 5 min, followed by 35 cycles of 94 °C for 30 s, 60 °C for 30 s and 72 °C for 60 s, and a final extension at 72 °C for 5 min. The PCR products were separated by electrophoresis on 2% agarose gels.

Histology

Lungs were embedded in paraffin using standard protocols. Then samples were cut into 8 µm sections, mounted on glass slides and stained with hematoxylin and eosin according to standard protocols. The histological analysis and score calculation were done by a pathologist in a blinded fashion. The histological score considers the presence or absence of edema, hemorrhage, congestion, immune cells in the tissue and the extent of all these parameters (Lartey, Vargas-Robles, et al. 2022; Lartey, Valle-Reyes, et al. 2022). A score of 0 indicates no inflammation; 1 low inflammation; 2 moderate inflammation; 3 high inflammation.

Determination of vascular permeability

For permeability assays in the lungs, arpin$^{+/+}$ and arpin$^{-/-}$ male mice, between 8 to 12 weeks old, were anesthetized and injected with 50 mg of 150 kDa FITC-dextran (Sigma-Aldrich) per 1 kg of body weight via the cannulated carotid artery. After 30

min, the mice were perfused with PBS to remove all the blood from the circulation. Then, lungs were collected, weighted, and homogenized in PBS. Fluorescence in the tissue was measured in a fluorometer and the mean fluorescence intensity (MFI) was normalized to tissue weight.

Modified Miles assays to measure vascular permeability in the skin was performed by injecting 8-12 weeks old arpin$^{+/+}$ and arpin$^{-/-}$ mice intraperitoneally with 2% Evans Blue dye in PBS. After 2 hours, mice were anesthetized and 100 µL of PBS containing either 450 ng histamine, 10 µM ROCK1/2 inhibitor Y27632, 10 µM ZIPK inhibitor HS38, 100 µM Arp2/3 complex inhibitor CK-666, or PBS (control) were intradermally injected into the shaved back skin. After 30 min, mice were sacrificed and the skin around the injection sites were excised. The skin pieces were incubated separately in formamide for 24 h to extract the blue dye and then read spectrophotometrically at 600 nm. Tissues were dried for eight days at RT and subsequently weighted. The densitometry values at 600 nm were divided by tissue weight and normalized to the values of the arpin$^{+/+}$ mice.

Blood leukocyte counts

Whole blood was collected from anesthetized mice by heart puncture with heparin as anti-coagulant. Blood samples were analyzed using an Exigo Veterinary Hematology System (Stockholm, Sweden) according to manufacturer's instructions.

Statistics

Statistical analyses were performed using Prism 8.0 software (GraphPad). Significance between two groups was assessed by two-tailed Student's t-test or

two-tailed Student's t-test with Welch's correction. Two-way ANOVA was performed for multiple group comparisons. For the mating statistics, χ^2 tests were performed to test the probability of the deviation between the observed and the expected values.

SUPPLEMENTAL MATERIAL

Supplemental Figure 1. Arpin is reduced by IL-1β.

Supplemental Figure 2. Arpin does not participate in junction assembly.

Supplemental Figure 3. Arpin deficiency increases vascular permeability in skin and alters venular junction architecture in cremaster muscle.

Supplemental Table S1. Mating statistics of arpin$^{+/-}$ mice.

Supplemental Table S2. Hemograms of arpin$^{+/+}$ and arpin$^{-/-}$ mice.

ACKNOWLEDGEMENTS

This project was funded by the Mexican National Council for Science and Technology (Consejo Nacional de Ciencia y Tecnología, CONACyT, Basic Science Project 284292 to MS). We thank all veterinarians in the animal facility of Cinvestav-IPN for taking care of all the mice; and the confocal microscopy unit at Cinvestav-IPN for helping with image acquisition. We also thank Dr. Klemens Rottner and Dr. Theresia Stradal (Technical University Braunschweig and Helmholtz Center for Infection Research, Braunschweig, Germany) for providing antibodies against arpC5 and cortactin; and Dr. Manuel Hernández-Hernández, Department of Cell Biology, Cinvestav-IPN, for proving antibodies against actin.

AUTHOR CONTRIBUTIONS

AM-G performed experiments and statistical analysis, analyzed, and interpreted data, and wrote the manuscript. IG-F, SC-P, KH-A, IL-V, AS-O, AB, and HV-R performed experiments and analyzed data. RM-F and MM-G generated the arpin antibody and analyzed data. CS-L analyzed histology samples and interpreted data. MS conceived and supervised the study, analyzed and interpreted data, obtained funding, and wrote the manuscript. All authors approved the final manuscript.

REFERENCES

Abu Taha, A., M. Taha, J. Seebach, and H. J. Schnittler. 2014. 'ARP2/3-mediated junction-associated lamellipodia control VE-cadherin-based cell junction dynamics and maintain monolayer integrity', *Mol Biol Cell*, 25: 245-56.

Angulo-Urarte, A., P. Casado, S. D. Castillo, P. Kobialka, M. P. Kotini, A. M. Figueiredo, P. Castel, V. Rajeeve, M. Mila-Guasch, J. Millan, C. Wiesner, H. Serra, L. Muixi, O. Casanovas, F. Vinals, M. Affolter, H. Gerhardt, S. Huveneers, H. G. Belting, P. R. Cutillas, and M. Graupera. 2018. 'Endothelial cell rearrangements during vascular patterning require PI3-kinase-mediated inhibition of actomyosin contractility', *Nat Commun*, 9: 4826.

Belvitch, P., M. E. Brown, B. N. Brinley, E. Letsiou, A. N. Rizzo, J. G. N. Garcia, and S. M. Dudek. 2017. 'The ARP 2/3 complex mediates endothelial barrier function and recovery', *Pulm Circ*, 7: 200-10.

Chanez-Paredes, S., A. Montoya-Garcia, K. F. Castro-Ochoa, J. Garcia-Cordero, L. Cedillo-Barron, M. Shibayama, P. Nava, S. Flemming, N. Schlegel, A. M. Gautreau, H. Vargas-Robles, R. Mondragon-Flores, and M. Schnoor. 2021. 'The Arp2/3 Inhibitory Protein Arpin Is Required for Intestinal Epithelial Barrier Integrity', *Front Cell Dev Biol*, 9: 625719.

Chen, Y., R. Li, S. Shang, X. Yang, L. Li, W. Wang, and Y. Wang. 2021. 'Therapeutic Potential of TNFalpha and IL1beta Blockade for CRS/ICANS in CAR-T Therapy via Ameliorating Endothelial Activation', *Front Immunol*, 12: 623610.

Crampton, S. P., J. Davis, and C. C. Hughes. 2007. 'Isolation of human umbilical vein endothelial cells (HUVEC)', *J Vis Exp*: 183.

Dahl, J. P., J. Wang-Dunlop, C. Gonzales, M. E. Goad, R. J. Mark, and S. P. Kwak. 2003. 'Characterization of the WAVE1 knock-out mouse: implications for CNS development', *J Neurosci*, 23: 3343-52.

Dang, I., R. Gorelik, C. Sousa-Blin, E. Derivery, C. Guerin, J. Linkner, M. Nemethova, J. G. Dumortier, F. A. Giger, T. A. Chipysheva, V. D. Ermilova, S. Vacher, V. Campanacci, I. Herrada, A. G. Planson, S. Fetics, V. Henriot, V. David, K. Oguievetskaia, G. Lakisic, F. Pierre, A. Steffen, A. Boyreau, N. Peyrieras, K. Rottner, S. Zinn-Justin, J. Cherfils, I. Bieche, A. Y. Alexandrova, N. B. David, J. V. Small, J. Faix, L. Blanchoin, and A.

Gautreau. 2013. 'Inhibitory signalling to the Arp2/3 complex steers cell migration', *Nature*, 503: 281-4.

Dang, I., J. Linkner, J. Yan, D. Irimia, J. Faix, and A. Gautreau. 2017. 'The Arp2/3 inhibitory protein Arpin is dispensable for chemotaxis', *Biol Cell*, 109: 162-66.

Figueiredo, A. M., P. Barbacena, A. Russo, S. Vaccaro, D. Ramalho, A. Pena, A. P. Lima, R. R. Ferreira, M. A. Fidalgo, F. El-Marjou, Y. Carvalho, F. F. Vasconcelos, A. M. Lennon-Dumenil, D. M. Vignjevic, and C. A. Franco. 2021. 'Endothelial cell invasion is controlled by dactylopodia', *Proc Natl Acad Sci U S A*, 118.

Garcia-Ponce, A., A. F. Citalan-Madrid, M. Velazquez-Avila, H. Vargas-Robles, and M. Schnoor. 2015. 'The role of actin-binding proteins in the control of endothelial barrier integrity', *Thromb Haemost*, 113: 20-36.

Garcia Ponce, A., A. F. Citalan Madrid, H. Vargas Robles, S. Chanez Paredes, P. Nava, A. Betanzos, A. Zarbock, K. Rottner, D. Vestweber, and M. Schnoor. 2016. 'Loss of cortactin causes endothelial barrier dysfunction via disturbed adrenomedullin secretion and actomyosin contractility', *Sci Rep*, 6: 29003.

Hilfenhaus, G., D. P. Nguyen, J. Freshman, D. Prajapati, F. Ma, D. Song, S. Ziyad, M. Cuadrado, M. Pellegrini, X. R. Bustelo, and M. L. Iruela-Arispe. 2018. 'Vav3-induced cytoskeletal dynamics contribute to heterotypic properties of endothelial barriers', *J Cell Biol*, 217: 2813-30.

Jubrail, J., K. Africano-Gomez, F. Herit, A. Mularski, P. Bourdoncle, L. Oberg, E. Israelsson, P. R. Burgel, G. Mayer, D. M. Cunoosamy, N. Kurian, and F.

Niedergang. 2020. 'Arpin is critical for phagocytosis in macrophages and is targeted by human rhinovirus', *EMBO Rep*, 21: e47963.

Lartey, N. L., S. Valle-Reyes, H. Vargas-Robles, K. E. Jimenez-Camacho, I. M. Guerrero-Fonseca, R. Castellanos-Martinez, A. Montoya-Garcia, J. Garcia-Cordero, L. Cedillo-Barron, P. Nava, J. G. Filisola-Villasenor, D. Roa-Velazquez, D. I. Zavala-Vargas, E. Morales-Rios, C. Salinas-Lara, E. Vadillo, and M. Schnoor. 2022. 'ADAM17/MMP inhibition prevents neutrophilia and lung injury in a mouse model of COVID-19', *J Leukoc Biol*, 111: 1147-58.

Lartey, N. L., H. Vargas-Robles, I. M. Guerrero-Fonseca, A. Garcia-Ponce, C. Salinas-Lara, K. Rottner, and M. Schnoor. 2022. 'The Actin-Binding Protein Cortactin Promotes Sepsis Severity by Supporting Excessive Neutrophil Infiltration into the Lung', *Biomedicines*, 10.

Li, T., H. M. Zheng, N. M. Deng, Y. J. Jiang, J. Wang, and D. L. Zhang. 2017. 'Clinicopathological and prognostic significance of aberrant Arpin expression in gastric cancer', *World J Gastroenterol*, 23: 1450-57.

Li, Y., J. Qiu, T. Pang, Z. Guo, Y. Su, Q. Zeng, and X. Zhang. 2017. 'Restoration of Arpin suppresses aggressive phenotype of breast cancer cells', *Biomed Pharmacother*, 92: 116-21.

Lomakina, M. E., F. Lallemand, S. Vacher, N. Molinie, I. Dang, W. Cacheux, T. A. Chipysheva, V. D. Ermilova, L. de Koning, T. Dubois, I. Bieche, A. Y. Alexandrova, and A. Gautreau. 2016. 'Arpin downregulation in breast cancer is associated with poor prognosis', *Br J Cancer*, 114: 545-53.

MacArthur, D. G., J. T. Seto, S. Chan, K. G. Quinlan, J. M. Raftery, N. Turner, M. D. Nicholson, A. J. Kee, E. C. Hardeman, P. W. Gunning, G. J. Cooney, S. I.

Head, N. Yang, and K. N. North. 2008. 'An Actn3 knockout mouse provides mechanistic insights into the association between alpha-actinin-3 deficiency and human athletic performance', *Hum Mol Genet*, 17: 1076-86.

Mako, V., J. Czucz, Z. Weiszhar, E. Herczenik, J. Matko, Z. Prohaszka, and L. Cervenak. 2010. 'Proinflammatory activation pattern of human umbilical vein endothelial cells induced by IL-1beta, TNF-alpha, and LPS', *Cytometry A*, 77: 962-70.

Malek, R., and S. Soufi. 2023. 'Pulmonary Edema.' in, *StatPearls* (Treasure Island (FL)).

Millan, J., R. J. Cain, N. Reglero-Real, C. Bigarella, B. Marcos-Ramiro, L. Fernandez-Martin, I. Correas, and A. J. Ridley. 2010. 'Adherens junctions connect stress fibres between adjacent endothelial cells', *BMC Biol*, 8: 11.

Mong, P. Y., and Q. Wang. 2009. 'Activation of Rho kinase isoforms in lung endothelial cells during inflammation', *J Immunol*, 182: 2385-94.

Mooren, O. L., J. Li, J. Nawas, and J. A. Cooper. 2014. 'Endothelial cells use dynamic actin to facilitate lymphocyte transendothelial migration and maintain the monolayer barrier', *Mol Biol Cell*, 25: 4115-29.

Park, M., H. J. Kim, B. Lim, A. Wylegala, and M. Toborek. 2013. 'Methamphetamine-induced occludin endocytosis is mediated by the Arp2/3 complex-regulated actin rearrangement', *J Biol Chem*, 288: 33324-34.

Prasain, N., and T. Stevens. 2009. 'The actin cytoskeleton in endothelial cell phenotypes', *Microvasc Res*, 77: 53-63.

Punwani, D., B. Pelz, J. Yu, N. C. Arva, K. Schafernak, K. Kondratowicz, M. Makhija, and J. M. Puck. 2015. 'Coronin-1A: immune deficiency in humans and mice', *J Clin Immunol*, 35: 100-7.

Rao, X., X. Huang, Z. Zhou, and X. Lin. 2013. 'An improvement of the 2^(-delta delta CT) method for quantitative real-time polymerase chain reaction data analysis', *Biostat Bioinforma Biomath*, 3: 71-85.

Reglero-Real, N., B. Colom, J. V. Bodkin, and S. Nourshargh. 2016. 'Endothelial Cell Junctional Adhesion Molecules: Role and Regulation of Expression in Inflammation', *Arterioscler Thromb Vasc Biol*, 36: 2048-57.

Schachtner, H., M. Weimershaus, V. Stache, N. Plewa, D. F. Legler, U. E. Hopken, and T. Maritzen. 2015. 'Loss of Gadkin Affects Dendritic Cell Migration In Vitro', *PLoS One*, 10: e0143883.

Schnoor, M., F. P. Lai, A. Zarbock, R. Klaver, C. Polaschegg, D. Schulte, H. A. Weich, J. M. Oelkers, K. Rottner, and D. Vestweber. 2011. 'Cortactin deficiency is associated with reduced neutrophil recruitment but increased vascular permeability in vivo', *J Exp Med*, 208: 1721-35.

Snapper, S. B., F. Takeshima, I. Anton, C. H. Liu, S. M. Thomas, D. Nguyen, D. Dudley, H. Fraser, D. Purich, M. Lopez-Ilasaca, C. Klein, L. Davidson, R. Bronson, R. C. Mulligan, F. Southwick, R. Geha, M. B. Goldberg, F. S. Rosen, J. H. Hartwig, and F. W. Alt. 2001. 'N-WASP deficiency reveals distinct pathways for cell surface projections and microbial actin-based motility', *Nat Cell Biol*, 3: 897-904.

Steinberg, J. P., K. Takamiya, Y. Shen, J. Xia, M. E. Rubio, S. Yu, W. Jin, G. M. Thomas, D. J. Linden, and R. L. Huganir. 2006. 'Targeted in vivo mutations

of the AMPA receptor subunit GluR2 and its interacting protein PICK1 eliminate cerebellar long-term depression', *Neuron*, 49: 845-60.

Tojkander, S., G. Gateva, and P. Lappalainen. 2012. 'Actin stress fibers--assembly, dynamics and biological roles', *J Cell Sci*, 125: 1855-64.

van der Kammen, R., J. Y. Song, I. de Rink, H. Janssen, S. Madonna, C. Scarponi, C. Albanesi, W. Brugman, and M. Innocenti. 2017. 'Knockout of the Arp2/3 complex in epidermis causes a psoriasis-like disease hallmarked by hyperactivation of transcription factor Nrf2', *Development*, 144: 4588-603.

Viita, T., S. Kyheroinen, B. Prajapati, J. Virtanen, M. J. Frilander, M. Varjosalo, and M. K. Vartiainen. 2019. 'Nuclear actin interactome analysis links actin to KAT14 histone acetyl transferase and mRNA splicing', *J Cell Sci*, 132.

Waschke, J., F. E. Curry, R. H. Adamson, and D. Drenckhahn. 2005. 'Regulation of actin dynamics is critical for endothelial barrier functions', *Am J Physiol Heart Circ Physiol*, 288: H1296-305.

Wojciak-Stothard, B., A. Entwistle, R. Garg, and A. J. Ridley. 1998. 'Regulation of TNF-alpha-induced reorganization of the actin cytoskeleton and cell-cell junctions by Rho, Rac, and Cdc42 in human endothelial cells', *J Cell Physiol*, 176: 150-65.

Yae, K., V. W. Keng, M. Koike, K. Yusa, M. Kouno, Y. Uno, G. Kondoh, T. Gotow, Y. Uchiyama, K. Horie, and J. Takeda. 2006. 'Sleeping beauty transposon-based phenotypic analysis of mice: lack of Arpc3 results in defective trophoblast outgrowth', *Mol Cell Biol*, 26: 6185-96.

Zeng, W., Z. Sun, T. Ma, X. Song, S. Li, Q. Zhang, W. Yuan, J. Li, L. Liu, M. Zhu, and H. Chen. 2021. 'Elevated ZIPK is required for TNF-alpha-induced cell

adhesion molecule expression and leucocyte adhesion in endothelial cells', *Acta Biochim Biophys Sin (Shanghai)*, 53: 567-74.

Zhang, S. R., H. Li, W. Q. Wang, W. Jin, J. Z. Xu, H. X. Xu, C. T. Wu, H. L. Gao, S. Li, T. J. Li, W. H. Zhang, S. S. Xu, Q. X. Ni, X. J. Yu, and L. Liu. 2019. 'Arpin downregulation is associated with poor prognosis in pancreatic ductal adenocarcinoma', *Eur J Surg Oncol*, 45: 769-75.

Zhang, Y., C. Zhang, H. Zhang, W. Zeng, S. Li, C. Chen, X. Song, J. Sun, Z. Sun, C. Cui, X. Cao, L. Zheng, P. Wang, W. Zhao, Z. Zhang, Y. Xu, M. Zhu, and H. Chen. 2019. 'ZIPK mediates endothelial cell contraction through myosin light chain phosphorylation and is required for ischemic-reperfusion injury', *FASEB J*, 33: 9062-74.

FIGURE LEGENDS

Figure 1. Arpin is expressed in endothelial cells.

(A) End-point RT-PCR for *ARPIN* in the human microvascular endothelial cell line (HMEC-1) and human umbilical vein endothelial cells (HUVEC), *7SL* was used as housekeeping gene (top); and *Arpin* in the mouse brain endothelial cell line bEnd.3 and primary murine lung endothelial cells (MLEC); *Actb* was used as a

housekeeping gene (bottom). A representative gel of three independent experiments is shown.

(B) Representative western blot for arpin in HUVEC and HMEC-1. MW= molecular weight bands. The graph shows the quantification of the relative pixel intensity of the arpin band normalized to γ-tubulin as a loading control (n=4). Data are represented as mean ± standard error of the mean (SEM); ns: non-significant; two-tailed student's t-test.

(C) Representative immunostaining of arpin and VE-Cadherin in HUVEC to analyze arpin localization at cell-cell junctions (40x objective; scale bar = 20 µm). Magnified views of boxed regions are shown (4.3 digital zoom; scale bar = 5 µm). The graphs show the dashed line scans performed with ImageJ software along the white lines in the magnified images. Profiles of the pixel intensity means of arpin and VE-Cadherin across junctions (1), along mature junctions (2) and along immature junctions (3) are depicted. 25 images each were analyzed from three independent experiments.

(D) Representative immunostaining of arpin and PECAM-1 in postcapillary venules of mouse cremaster muscles to analyze arpin localization at cell-cell junctions *in vivo* (40x objective; scale bar = 20 µm). Magnified views of dashed boxed regions are shown (3.3x digital zoom; scale bar = 10 µm). The graphs show the line scans performed with ImageJ software along the white lines in the magnified images. Profiles of the pixel intensity means of arpin and PECAM-1 across junctions (1), and along mature junctions (2) are depicted. 15 venules each were analyzed from four mice.

Figure 2. Arpin is downregulated by TNFα.

(A) qRT-PCR for the Arp2/3 complex inhibitors *ARPIN*, *AP1AR* and *PICK1* using cDNA from HUVEC treated or not with TNFα for the indicated times (n=4). Data are shown as relative expression (fold change) normalized to the housekeeping gene *7SL.*

(B) Representative western blot for arpin in HUVEC treated or not with TNFα for the indicated times (n=5). MW= molecular weight bands. ICAM-1 was used as a positive control of the induction of inflammation. The graph shows the mean pixel intensity of arpin bands normalized to tubulin as loading control and to the control condition (set to 1).

(C) Representative **i**mmunostaining of arpin and VE-Cadherin together with phalloidin F-actin staining in HUVEC treated or not with TNFα for 4 h (40x Objective, scale bar = 20 µm). Magnifications on the right show the loss of arpin at junctions after TNFα treatment (orange arrows). The graphs show arpin pixel intensity quantification after treatment normalized to the average of ctrl HUVECs: top-left, total arpin in 17 images each was analyzed from four independent experiments; top-right, junctional and actin cytoskeletal arpin in 19 images each were analyzed from three independent experiments; and bottom graph: Pearson's correlation analysis showing that arpin is inversely correlated to central actin fiber density (Pearson's correlation coefficient, r; 49 cells were analyzed from three independent experiments).

(D) Representative immunostaining for arpin (blue) and PECAM-1 (red) in postcapillary venules treated or not with TNFα at the indicated times. PECAM-1 and MRP14 (neutrophils) stainings (right) are shown as positive control for the induction of inflammation (40x objective, scale bar = 20 µm). The top graph shows

total arpin pixel intensity quantification after TNFα treatment normalized to the average of control venules (12-14 venules were analyzed from four mice in each group). The bottom graph shows junctional and non-junctional arpin quantification after TNFα treatment normalized to the average of control venules (12-14 venules were analyzed from four mice in each group).

All data are represented as mean ± SEM; *p<0.05; **p<0.01; ***p<0.001; ****p<0.0001; two-tailed student's t-test.

Figure 3. Arpin depletion induces hyperpermeability and irregular junction patterns.

(A) Representative Western blots for WAVE2, WASP, the Arp2/3 subunit ArpC5 and arpin in lysates of control (shCtrl) and arpin-depleted (shArpin) HUVEC. The graph shows the mean pixel intensities of the protein bands normalized to the respective control bands. All bands were normalized to γ-tubulin as loading control (n=3).

(B) Paracellular flux of 150 kDa FITC-dextran across confluent control and arpin-depleted HUVEC monolayers cultured on transwell filters (0.4μm pore size) untreated or treated with TNFα for 18 h. Data are represented as relative permeability normalized to control HUVEC set to 1 (n=9 in three independent experiments).

(C) Representative Western blots for VE-Cadherin, β-catenin, vinculin, and arpin in lysates of control and arpin-depleted HUVEC. The graph shows the mean pixel intensities of the protein bands normalized to the respective control bands (set to 1). All bands were normalized to γ-tubulin as a loading control (n=3)**.**

(D) Representative Western blots for ZO-1, claudin-5 and arpin in lysates of control and arpin-depleted HUVEC. γ-Tubulin was used as a loading control. The graph shows the quantification of the relative pixel intensity of ZO-1 and claudin-5 bands normalized to the untreated control (set to 1) and γ-tubulin (n=3).

(E) Immunostaining of VE-Cadherin and β-catenin in control and arpin-depleted HUVEC (40x objective, scale bar = 20 µm; dashed boxes indicate magnified areas that highlight changes in junctional architecture; 3.3 digital zoom, scale bars = 5 µm). Representative images of four independent experiments are shown. Arrows depict linear and mature junctions in shctrl HUVEC and interrupted and gap junction formation and junction internalization in shArpin HUVEC.

All data are represented as mean ± SEM; ns: non-significant; *$p<0.05$; ***$p<0.001$; ****$p<0.0001$; two-tailed student's t-test.

Figure 4. Arpin depletion induces actin filament formation.

(A) Representative F-actin staining using phalloidin of control and arpin-depleted HUVEC (40x objective, scale bar = 20µm). The graph shows phalloidin pixel intensity quantification normalized to the average of control HUVEC. 18 images were analyzed in each group from four independent experiments.

(B) Representative immunostaining of VE-Cadherin with F-actin staining using phalloidin (top) in control and arpin-depleted HUVEC. The method of central actin fiber quantification using the phalloidin signal is depicted on the bottom as reported before (Garcia Ponce et al. 2016) (63x objective, scale bar = 5 µm). Yellow dashed lines delineate an individual cell. The graph shows the mean central actin fiber density quantification along the orange lines. 109 cells were analyzed in each group from 3 independent experiments.

(C) Representative Western blot for total actin in lysates of control and arpin-depleted HUVEC. The graph shows the mean pixel intensity of the actin bands normalized to the control and to γ-tubulin as a loading control (n=4).

(D) Representative Western blots for cortactin, coronin1B, p-cofilin, cofilin and arpin in lysates of control and arpin-depleted HUVEC. The graph shows the mean pixel intensity of the protein bands normalized to the respective control bands (set to 1). All bands were normalized to γ-tubulin as a loading control (n=4).

All data are represented as mean ± SEM; ns: non-significant; **p<0.01; ****p<0.0001; two-tailed student's t-test.

Figure 5. Inhibition of Arp2/3 complex in arpin-depleted HUVEC does not rescue hyperpermeability and actin cytoskeleton alterations.

(A) Immunostaining of VE-Cadherin with F-actin staining using phalloidin in control and arpin-depleted HUVEC treated with 100 µM of the Arp2/3 inhibitor CK-666 or vehicle (40x objective, scale bar = 20 µm). Representative images of three independent experiments are shown.

(B) Total phalloidin pixel intensity quantification normalized to the average of control HUVEC. 9 images were analyzed in each group from three independent experiments.

(C) Central actin fiber density quantification done as described in figure 4B. 100 cells were analyzed in each group from three independent experiments.

(D) Paracellular flux assays using confluent control and arpin-depleted HUVEC monolayers on 0.4 µm pore transwell filters treated with 100 µM CK-666 or vehicle (n=7-9 from three independent experiments). Data are normalized to control HUVEC treated with vehicle set to 1.

All data are represented as mean ± SEM; *p<0.05; **p<0.01; ***p<0.001; ****p<0.0001; two-tailed student's t-test.

Figure 6. Arpin depletion increases the formation of actin stress fibers.

(A) Representative Western blots for pMLC (Ser19), MLC and arpin in lysates of control and arpin-depleted HUVEC. The graph shows the mean pixel intensity of the protein bands normalized to the respective control band (set to 1). All bands were normalized to γ-tubulin as a loading control (n=4).

(B) Representative Western blots for pMYPT1 (Thr696), pMYPT1 (Thr853), MYPT1, and arpin in lysates of control and arpin-depleted HUVEC. The graph shows the mean pixel intensity of the protein bands normalized to the respective control band (set to 1). All bands were normalized to γ-tubulin as a loading control (n=4).

(C) Representative Western blots for ROCK1, mDia, ZIPK, and arpin in lysates of control and arpin-depleted HUVEC. The graph shows the mean pixel intensity of the protein bands normalized to the respective control band (set to 1). All bands were normalized to γ-tubulin as a loading control (n=4).

All data are represented as mean ± SEM; ns: non-significant; *p<0.05; **p<0.01; ***p<0.001; two-tailed student's t-test.

Figure 7. ROCK1/2 and ZIPK inhibition partially rescues increase in stress fibers and permeability in arpin-depleted HUVEC.

(A) Representative immunostaining of VE-Cadherin with F-actin staining using phalloidin in control and arpin-depleted HUVEC treated or not with 10 μM of the ROCK1/2 inhibitor Y27632 (40x objective, scale bar = 20μm).

(B) Phalloidin pixel intensity quantification normalized to the average of control HUVEC. 14 images were analyzed in each group from three independent experiments.

(C) Central actin fiber density quantification of at least 140 cells in each group from three independent experiments.

(D) Paracellular flux assays using confluent control and arpin-depleted HUVEC monolayers on 0.4 µm pore transwell filters treated with 10 µM Y27632 or vehicle (n=10-12 from four independent experiments).

(E) Representative immunostaining of VE-Cadherin with F-actin staining using phalloidin in control and arpin-depleted HUVEC treated with 10 µM of the ZIPK inhibitor HS38 or vehicle (40x objective; scale bar = 20µm).

(F) Phalloidin pixel intensity quantification normalized to the average of control HUVEC treated with the vehicle. 13 images were analyzed in each group from three independent experiments.

(G) Central actin fiber density quantification of at least 125 cells in each group from three independent experiments.

(H-I) Paracellular flux assays using confluent control and arpin-depleted HUVEC monolayers on 0.4 µm pore transwell filters treated with **(H)** 10 µM HS38 or vehicle (n=9-12 in four independent experiments) or **(I)** treated or not with 15 ng/mL TNFα and with 10 µM HS38 or vehicle (7-8 in three independent experiments).

All immunofluorescences are representative of three independent experiments. All data are represented as mean ± SEM; ns: non-significant; *$p<0.05$; **$p<0.01$; ***$p<0.001$; ****$p<0.0001$; two-tailed student's t-test.

Figure 8. Arpin-deficient mice are viable but show increased vascular permeability in the lung and skin.

(A) Arpin mouse gene showing exon 3, which was deleted using the CRISP/Cas9 technology to generate the complete arpin$^{-/-}$ mouse model.

(B) Representative genotypification PCR of mice carrying the WT (arpin$^{+/+}$), heterozygous (arpin$^{+/-}$), and deleted (KO, arpin $^{-/-}$) alleles.

(C) Representative Western blots for arpin in lysates of the indicated organ tissues from arpin$^{+/+}$ and arpin$^{-/-}$ mice (n=3).

(D) Permeability assays in the lungs. 150 kDa FITC-dextran was injected into arpin$^{+/+}$ and arpin$^{-/-}$ mice via the cannulated artery carotid. Animals were sacrificed, perfused, and lungs collected and homogenized in PBS. The homogenized tissue containing the leaked FITC-dextran was quantified using a fluorometer. (5 arpin$^{+/+}$ and 8 arpin$^{-/-}$ mice were analyzed). Data are represented as mean ± SEM; *$p<0.05$; two-tailed student's t-test with Welch's correction.

(E) Miles assays to determine vascular permeability in the back skin of arpin$^{+/+}$ and arpin$^{-/-}$ mice under basal conditions and after treatment with histamine, 10 μM ROCK1/2 inhibitor Y27632, 10 μM ZIPK inhibitor HS38, 100 μM Arp2/3 complex inhibitor CK-666, or PBS only as control. Data are shown as relative permeability normalized to the untreated arpin$^{+/+}$ group set to 1 (n = at least 7 mice in each group), and represented as means ± SEM. **$p<0.01$; ***$p<0.001$; ****$p<0.0001$; two-tailed student's t-test.

(F) Representative images of the hematoxylin and eosin staining of lung tissues of arpin$^{+/+}$ (images 1 and 2) and arpin$^{-/-}$ (images 3-6) mice. Image 1 shows normal

histology (10x objective). Image 2 shows normal structure of alveoli (*) and the blood vessels (arrowheads) without any pathology (40x objective, images 2-6). Image 3 shows some areas with alveolar volume reduced (*) in arpin$^{-/-}$ mice. Image 4 shows discrete interalveolar hemorrhages (arrow heads). Image 5 shows congestion and dilatation of the capillaries (arrow heads). Image 6 shows interalveolar edema (*) and microhemorrhage (arrowhead). The histological score of the lung tissue is shown in the graph below. A score of 0 indicates no inflammation; 1 low inflammation; 2 moderate inflammation; 3 high inflammation (9 images from arpin$^{+/+}$ and 12 images from arpin$^{-/-}$ mice were analyzed). Data are represented as mean ± SEM; *$p<0.05$; two-tailed student's t-test.

(G) Representative immunostaining for PECAM-1 and F-actin staining using phalloidin in cryosections from lungs of arpin$^{+/+}$ and arpin$^{-/-}$ mice. Images in the bottom shown endothelial cell (EC) F-actin extracted using PECAM-1 as a templete of ECs using Imaris software (40x objective, scale bar = 50µm). Graph shows mean F-actin pixel intensity quantification in arpin$^{-/-}$ lungs normalized to the average of images from arpin$^{+/+}$ lungs (20 images were analyzed from three mice in each group). Data are represented as mean ± SEM; **$p<0.01$; two-tailed student's t-test.

Figure 9. Current working model for arpin functions in ECs.

Under basal conditions arpin is located throughout the cell and enriched at cellular junctions. During inflammation, arpin is downregulated causing the formation of actomyosin actin stress fibers, junction disruption, and increased permeability. Question marks indicate the hitherto unknown mechanism of how arpin controls

the activity of ROCK and ZIPK to induce the formation of contractile actin stress fibers.

Supplemental figure legends

Supplemental Figure 1. Arpin is reduced by IL-1β.

(A) Representative Western blot for PICK1 in HUVEC treated or not with TNFα for the indicated times (n=3). The graph shows the mean pixel intensity of PICK1 bands normalized to tubulin as loading control and to the control condition (set to 1).

(B) Representative Western blot for arpin in HUVEC treated or not with IL-1β for the indicated times. ICAM-1 was used as a positive control of the induction of inflammation. The graph shows the quantification of the relative pixel intensity of arpin bands normalized to the untreated control (set to 1) and γ-tubulin as a loading control (n=4).

(C) Representative Western blot for PICK1 in HUVEC treated or not with IL-1 β for the indicated times (n=3). The graph shows the mean pixel intensity of PICK1 bands normalized to tubulin as loading control and to the control condition (set to 1).

(D) Representative immunostaining of VE-Cadherin and arpin with F-actin staining using phalloidin in HUVEC treated or not with IL-1β (Scale bar = 20µm). The upper left graph shows total arpin pixel intensity quantification normalized to the average of control HUVEC (top-left; n=11 in three independent experiments). The upper right graph shows junctional and actin cytoskeletal arpin quantification in control and IL-1β treatment HUVEC (n=11-15 in each group in three independent

experiments). Tho graph in the bottom shows that arpin is inversely correlated to central actin fiber density (Pearson's correlation coefficient, r, n=45 cells).

All data are represented as mean ± SEM; *p<0.05; **p<0.01; ***p<0.001; two-tailed student's t-test.

Supplemental Figure 2. Arpin does not participate in junction assembly.

(A) Representative immunostaining of VE-Cadherin in control and arpin-depleted HUVEC in calcium-switch assays over time (63x objective; scale Bar = 20 µm). The graph shows the quantification of junctional length, calculated in imageJ software, per number of cells (n=3).

All data are represented as mean ± SEM; *p<0.05; **p<0.01; ****p<0.0001; two-way ANOVA.

Supplemental Figure 3. Arpin deficiency increases vascular permeability in skin and alters venular junction architecture in cremaster muscle.

(A) The graph shows the average weight of arpin$^{+/+}$ and arpin $^{-/-}$ mice over time (at least 3 arpin$^{+/+}$ and arpin$^{-/-}$ mice were weighted at each time point).

(B) Representative Western blots for the indicated proteins in lysates of lung tissue from arpin$^{+/+}$ and arpin$^{-/-}$ mice. The graph shows the quantification of the relative pixel intensity of the protein bands normalized to γ-tubulin as a loading control (n=3).

(C) Representative immunostaining for arpin and VE-Cadherin in postcapillary venules of arpin$^{+/+}$ and arpin$^{-/-}$ mice. (n=3; dashed boxes indicate magnified areas, 40x objective; scale Bar = 20 µm). Arrows in the magnifications to the right show the altered junction architecture in the absence of arpin (4x digital zoom; scale Bar = 5 µm).

(D) Representative immunostaining for ZO-1 in postcapillary venules of arpin$^{+/+}$ and arpin $^{-/-}$ mice. (n=3; Dashed box indicate delineate magnified area, 40x objective; Scale Bar = 20µm), images from the right show junction architecture (4x digital zoom; Scale Bar = 10µm).

Figure 1

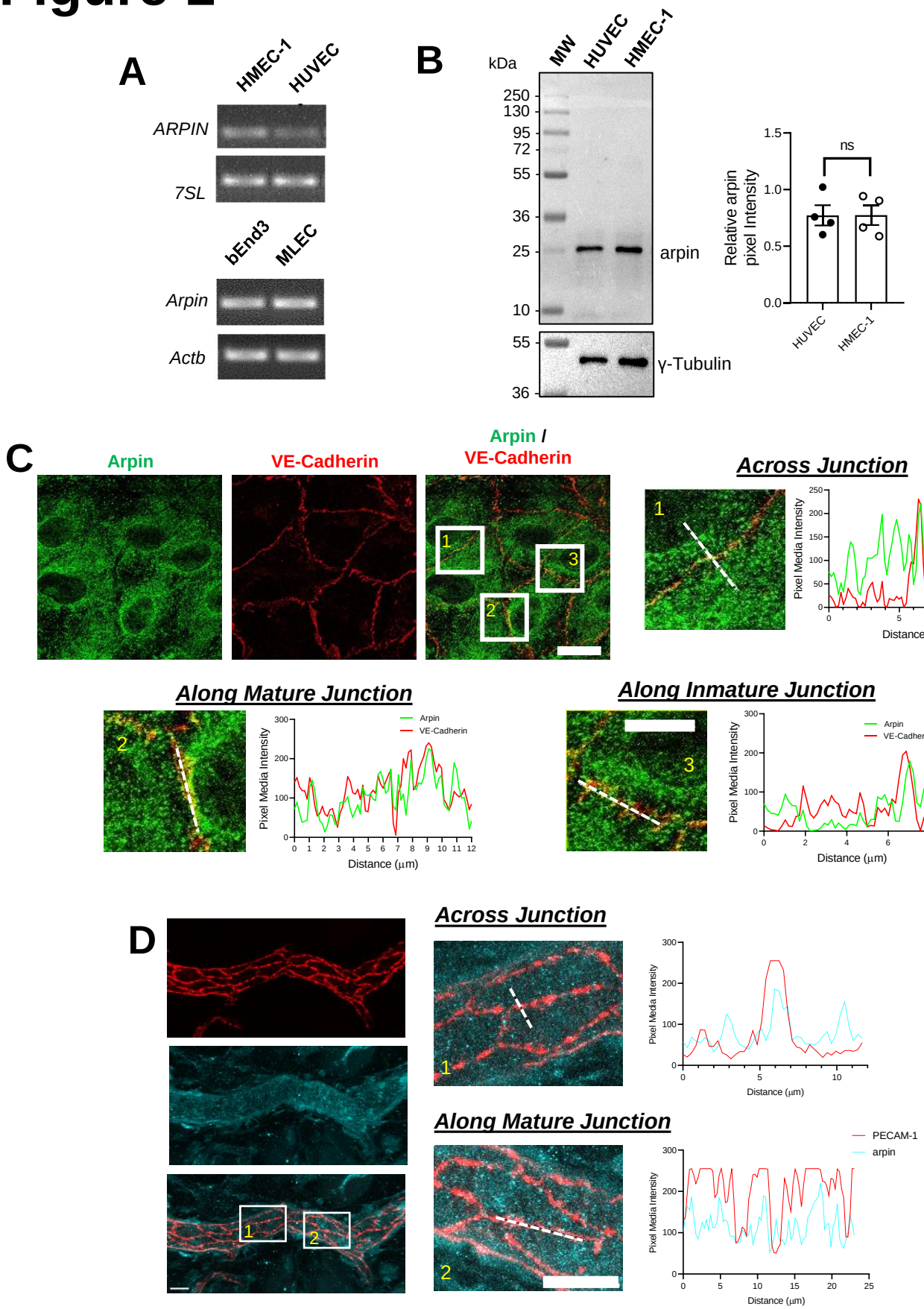
A
HMEC-1
HUVEC
ARPIN
7SL
bEnd3
MLEC
Arpin
Actb
B
kDa
MW
HUVEC
HMEC-1
250
130
95
72
55
36
25
10
arpin
55
36
γ-Tubulin
Relative arpin pixel Intensity
ns
HUVEC
HMEC-1
C
Arpin
VE-Cadherin
Arpin / VE-Cadherin
Across Junction
Pixel Media Intensity
Distance (μm)
Along Mature Junction
Along Inmature Junction
Arpin
VE-Cadherin
D
Across Junction
Along Mature Junction
PECAM-1
arpin

Figure 2

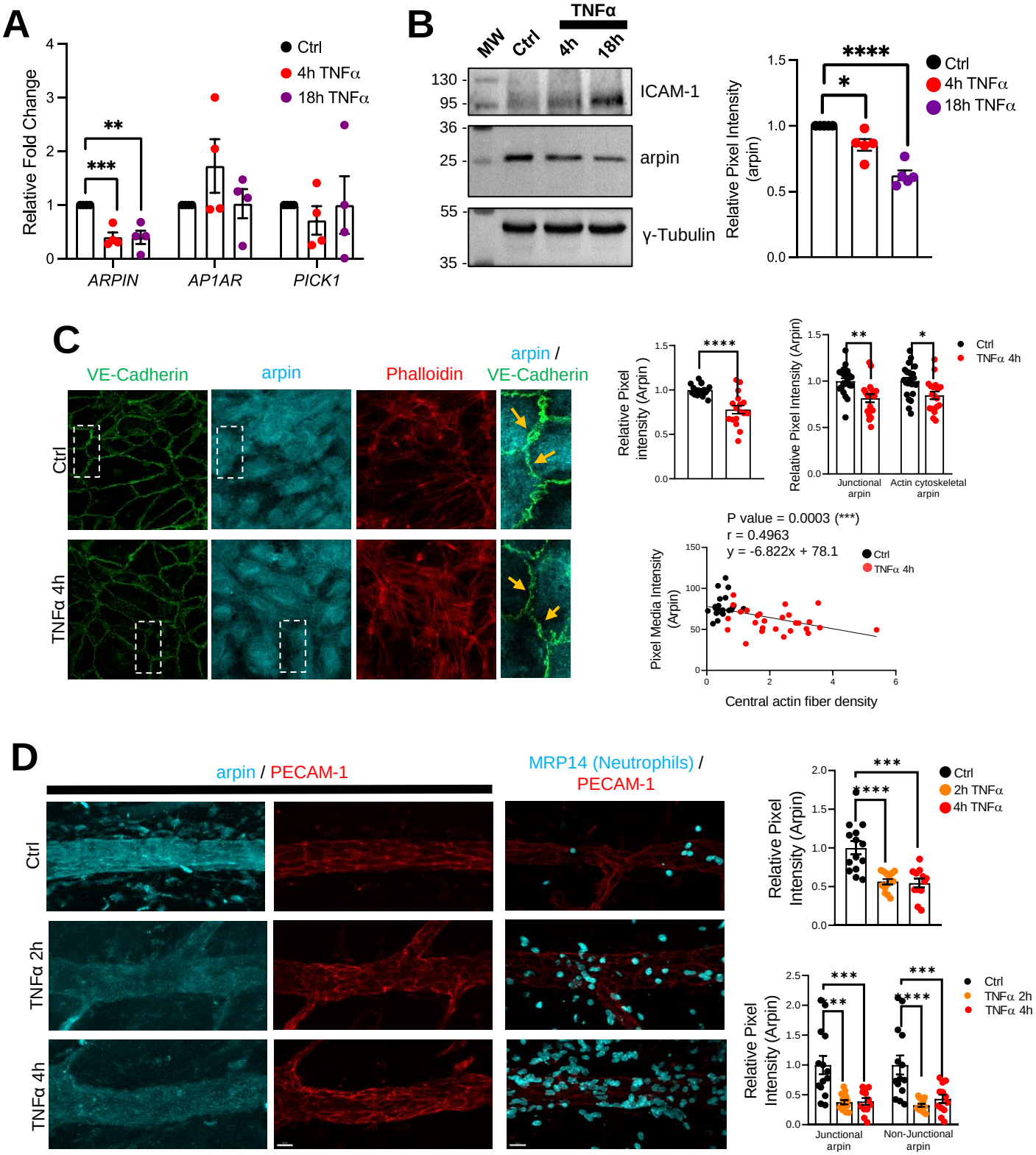
A
Relative Fold Change
Ctrl
4h TNFα
18h TNFα
**
***
ARPIN
AP1AR
PICK1
B
TNFα
MW
Ctrl
4h
18h
130
95
36
25
55
35
ICAM-1
arpin
γ-Tubulin
Relative Pixel Intensity (arpin)
****
*
C
VE-Cadherin
arpin
Phalloidin
arpin / VE-Cadherin
Ctrl
TNFα 4h
Relative Pixel intensity (Arpin)
Relative Pixel Intensity (Arpin)
Junctional arpin
Actin cytoskeletal arpin
P value = 0.0003 (***)
r = 0.4963
y = -6.822x + 78.1
Pixel Media Intensity (Arpin)
Central actin fiber density
D
arpin / PECAM-1
MRP14 (Neutrophils) / PECAM-1
Ctrl
TNFα 2h
TNFα 4h
Relative Pixel Intensity (Arpin)
2h TNFα
Junctional arpin
Non-Junctional arpin

Figure 3

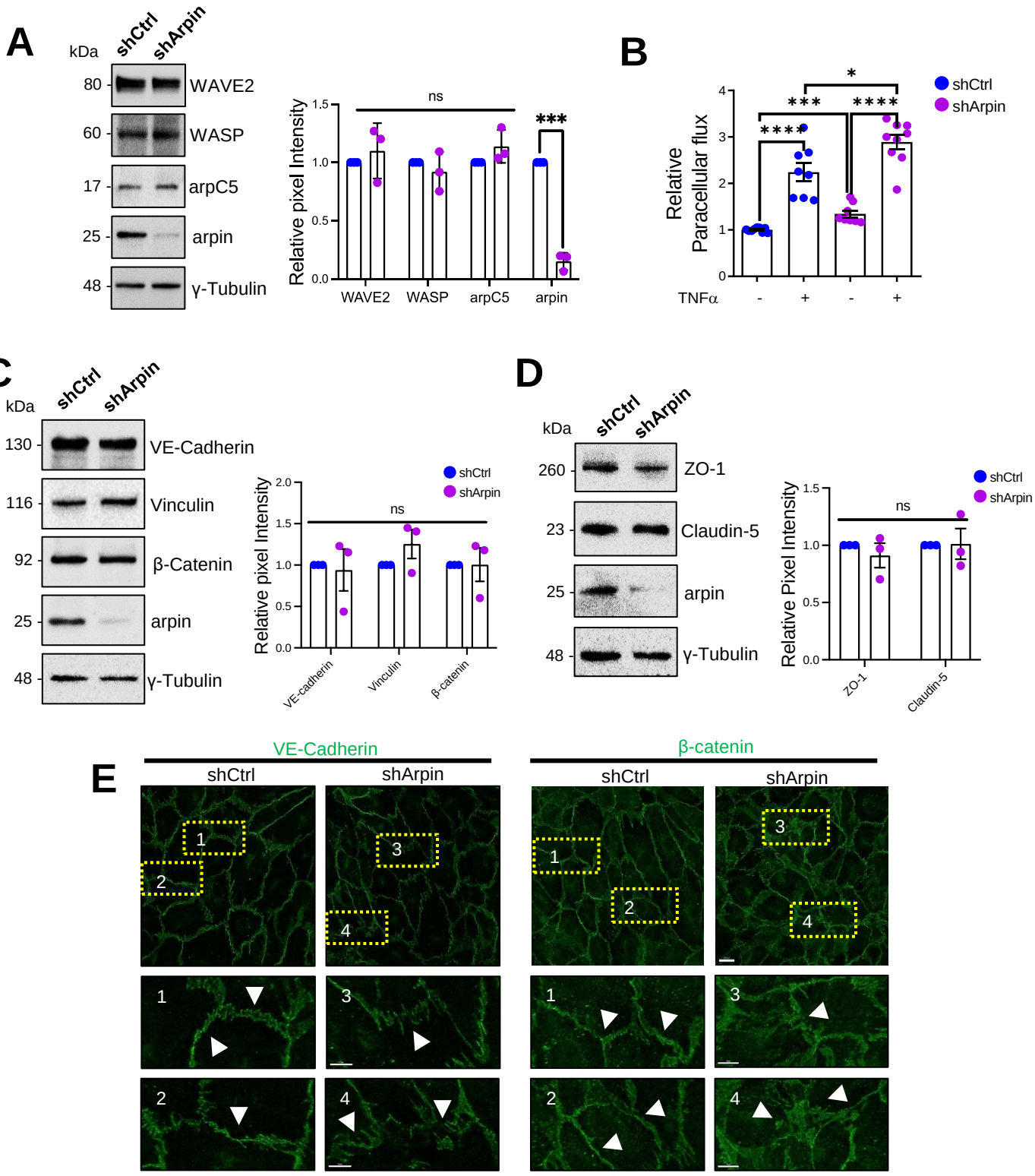
A
kDa
shCtrl
shArpin
80
WAVE2
60
WASP
17
arpC5
25
arpin
48
γ-Tubulin
Relative pixel Intensity
ns
***
WAVE2
WASP
arpC5
arpin
B
Relative Paracellular flux
shCtrl
shArpin
*
***
****
****
TNFα
-
+
-
+
C
kDa
shCtrl
shArpin
130
VE-Cadherin
116
Vinculin
92
β-Catenin
25
arpin
48
γ-Tubulin
Relative pixel Intensity
ns
VE-cadherin
Vinculin
β-catenin
D
kDa
shCtrl
shArpin
260
ZO-1
23
Claudin-5
25
arpin
48
γ-Tubulin
Relative Pixel Intensity
ns
ZO-1
Claudin-5
E
VE-Cadherin
β-catenin
shCtrl
shArpin
shCtrl
shArpin
1
2
3
4

Figure 4

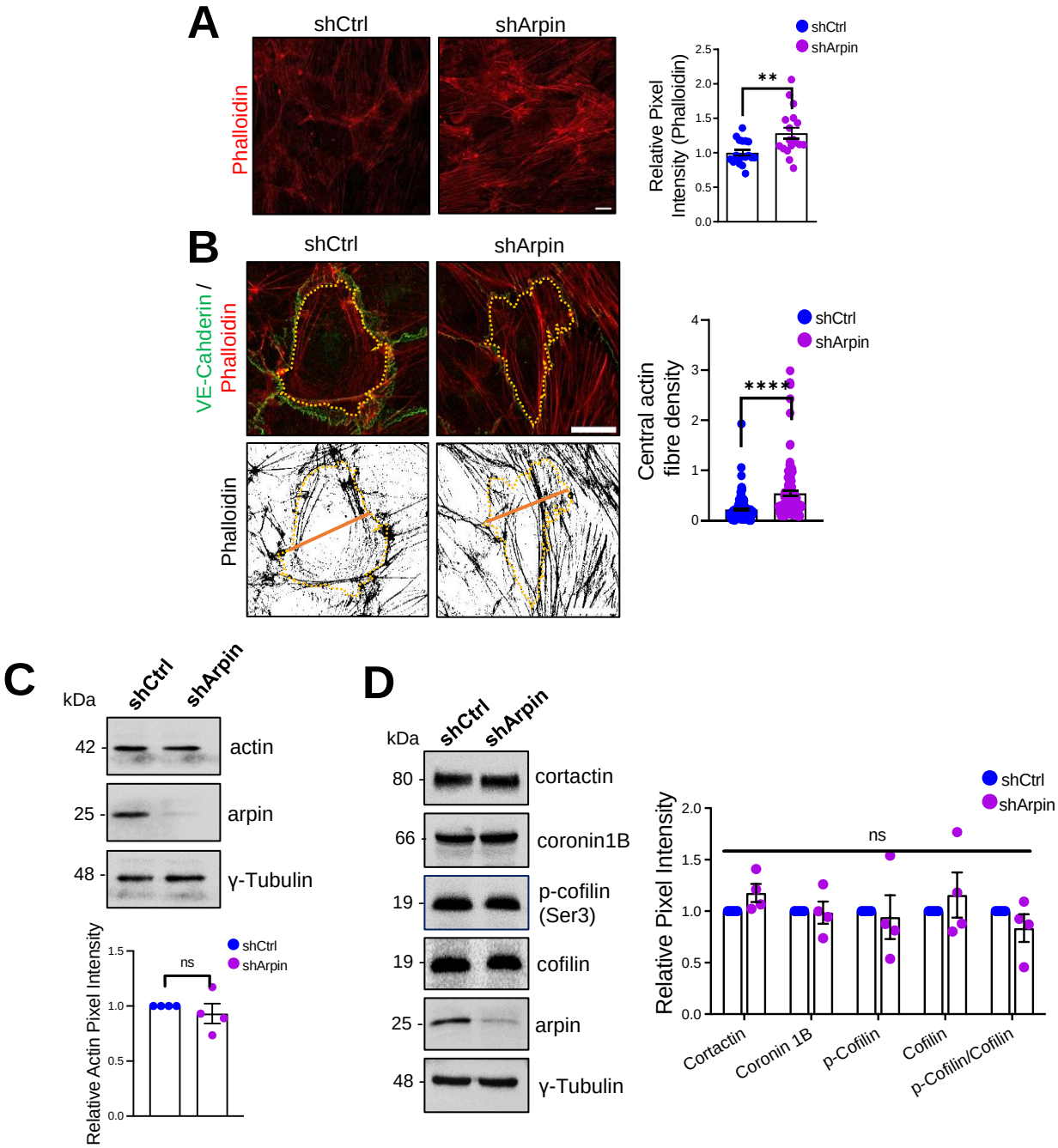
A
shCtrl
shArpin
Phalloidin
shCtrl
shArpin
Relative Pixel Intensity (Phalloidin)
**
B
shCtrl
shArpin
VE-Cahderin / Phalloidin
Phalloidin
shCtrl
shArpin
Central actin fibre density
****
C
kDa
shCtrl
shArpin
42
actin
25
arpin
48
γ-Tubulin
shCtrl
shArpin
Relative Actin Pixel Intensity
ns
D
kDa
shCtrl
shArpin
80
cortactin
66
coronin1B
19
p-cofilin (Ser3)
19
cofilin
25
arpin
48
γ-Tubulin
shCtrl
shArpin
Relative Pixel Intensity
ns
Cortactin
Coronin 1B
p-Cofilin
Cofilin
p-Cofilin/Cofilin

Figure 5

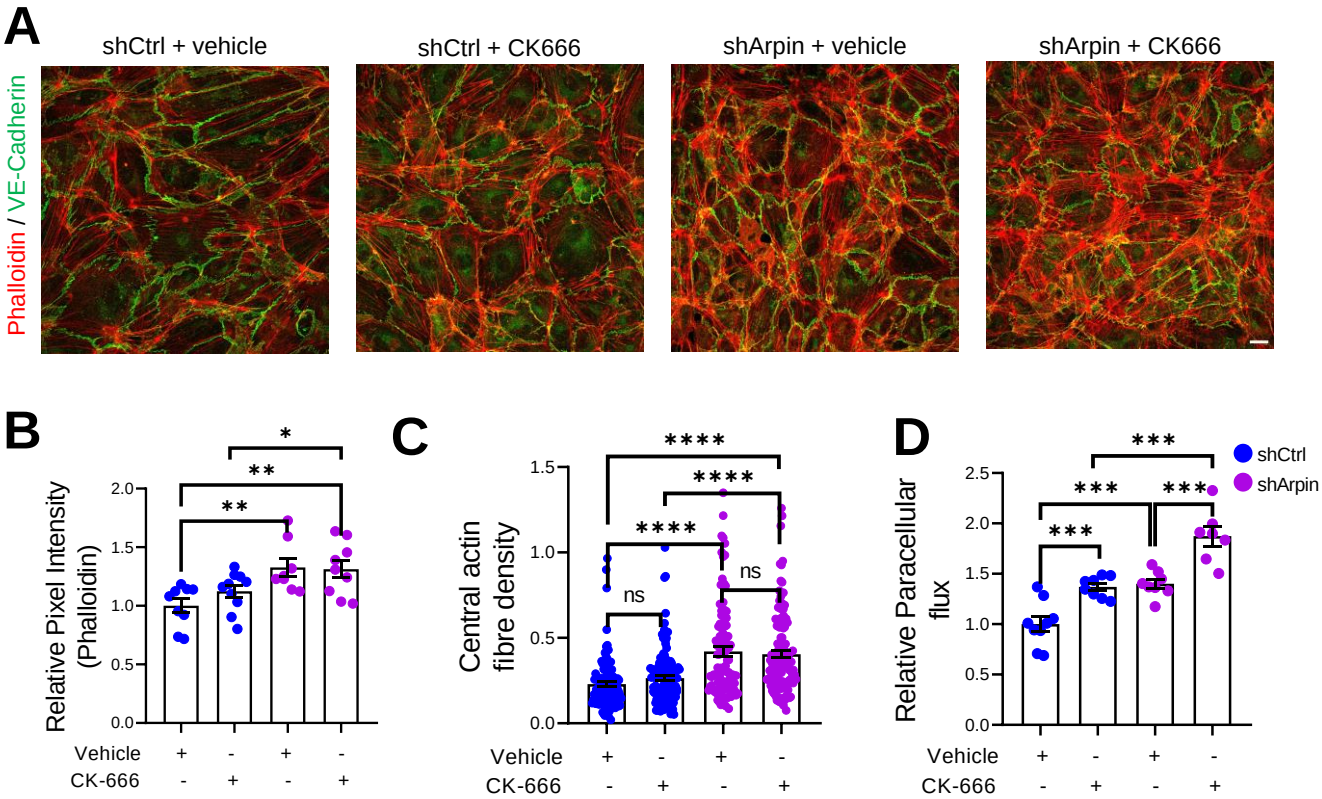
A
shCtrl + vehicle
shCtrl + CK666
shArpin + vehicle
shArpin + CK666
Phalloidin / VE-Cadherin
B
Relative Pixel Intensity (Phalloidin)
2.0
1.5
1.0
0.5
0.0
*
**
**
Vehicle + - + -
CK-666 - + - +
C
Central actin fibre density
1.5
1.0
0.5
0.0
****
****
****
ns
ns
Vehicle + - + -
CK-666 - + - +
D
Relative Paracellular flux
2.5
2.0
1.5
1.0
0.5
0.0
***
***
***
***
shCtrl
shArpin
Vehicle + - + -
CK-666 - + - +

Figure 6

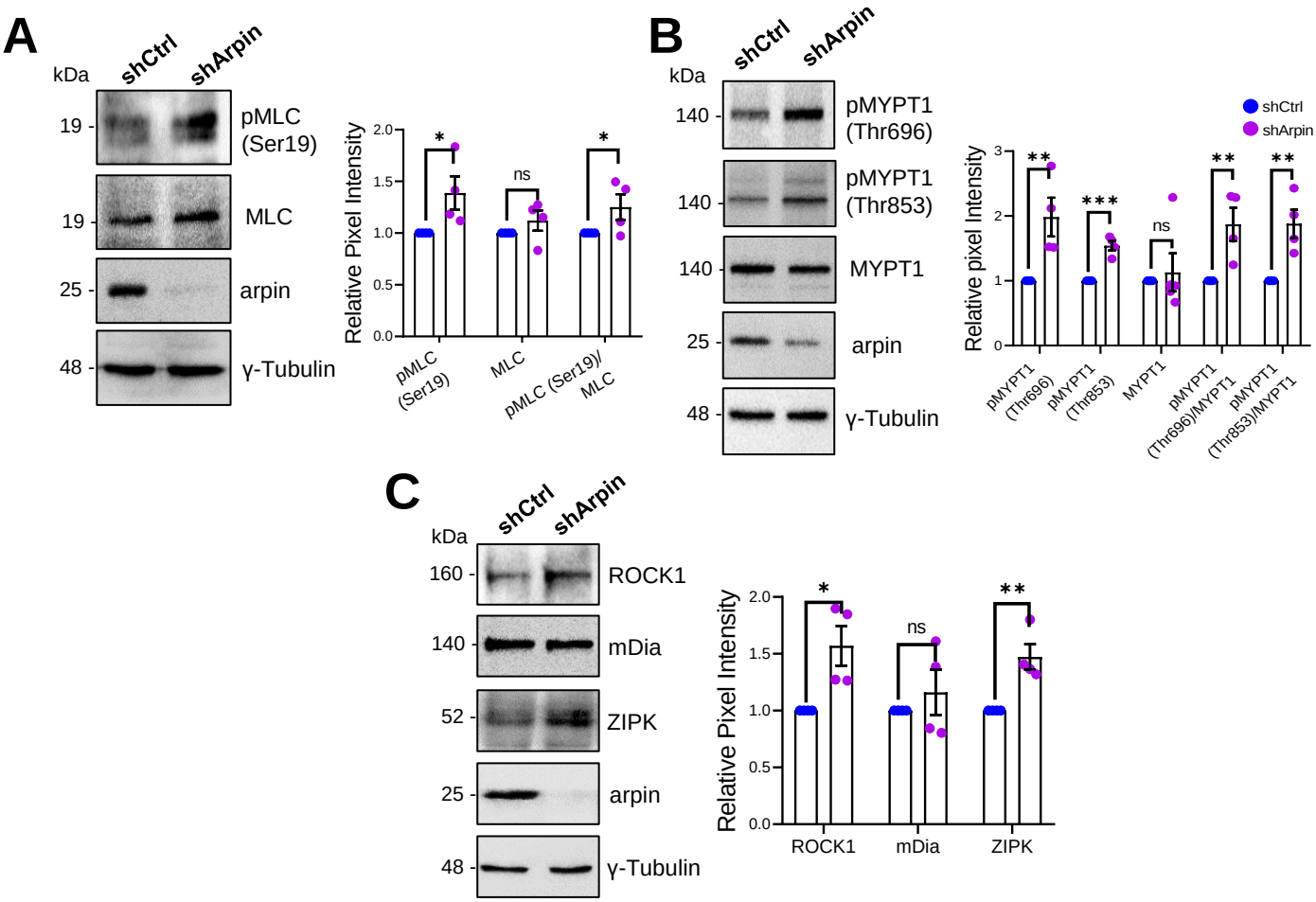
A
kDa
shCtrl
shArpin
19
pMLC (Ser19)
19
MLC
25
arpin
48
γ-Tubulin
Relative Pixel Intensity
2.0
1.5
1.0
0.5
0.0
*
ns
*
pMLC (Ser19)
MLC
pMLC (Ser19)/ MLC
B
kDa
shCtrl
shArpin
140
pMYPT1 (Thr696)
140
pMYPT1 (Thr853)
140
MYPT1
25
arpin
48
γ-Tubulin
shCtrl
shArpin
Relative pixel Intensity
3
2
1
0
**
***
ns
**
**
pMYPT1 (Thr696)
pMYPT1 (Thr853)
MYPT1
pMYPT1 (Thr696)/MYPT1
pMYPT1 (Thr853)/MYPT1
C
kDa
shCtrl
shArpin
160
ROCK1
140
mDia
52
ZIPK
25
arpin
48
γ-Tubulin
Relative Pixel Intensity
2.0
1.5
1.0
0.5
0.0
*
ns
**
ROCK1
mDia
ZIPK

Figure 7

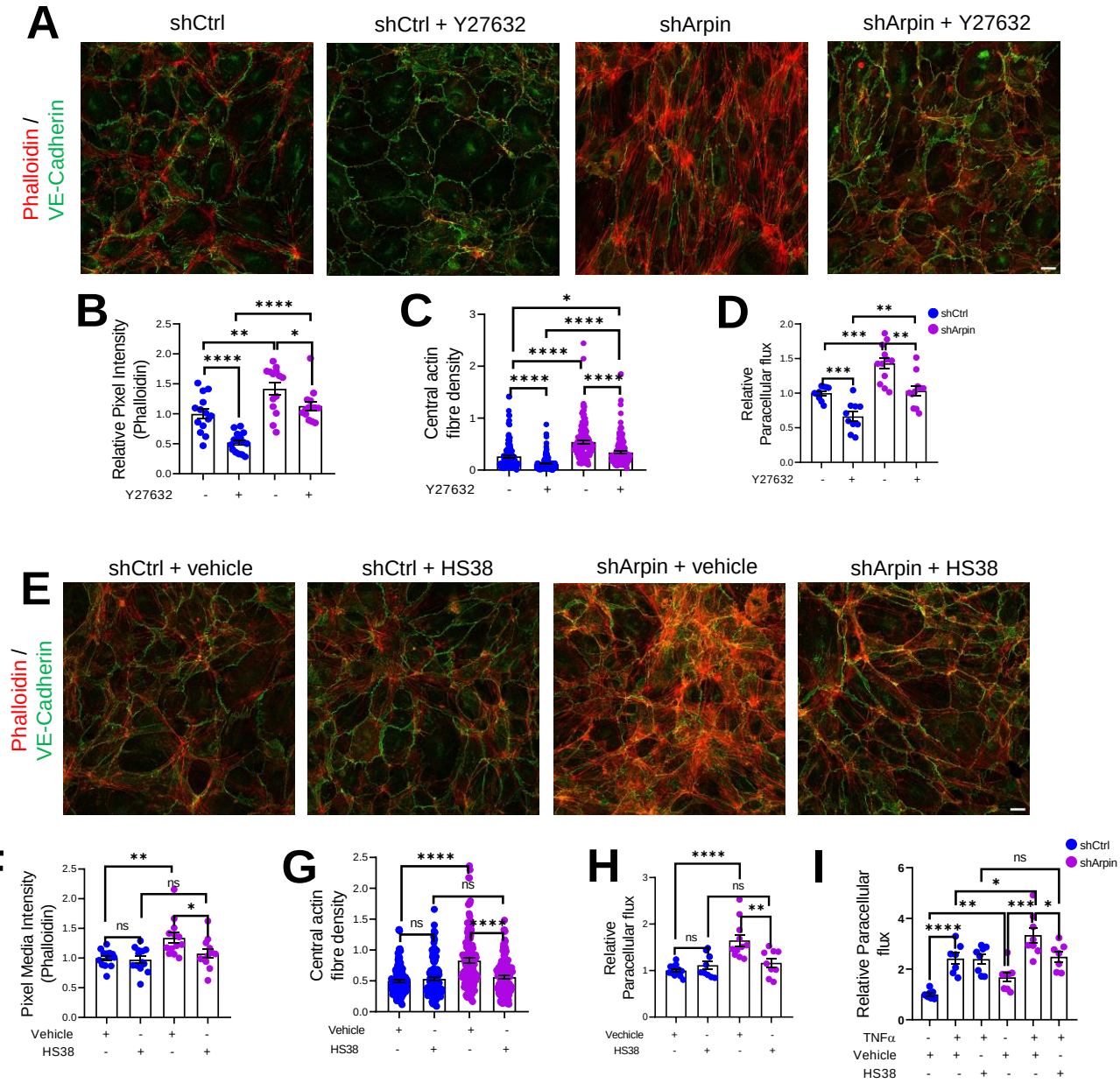
A
shCtrl
shCtrl + Y27632
shArpin
shArpin + Y27632
Phalloidin / VE-Cadherin
B
Relative Pixel Intensity (Phalloidin)
Y27632
C
Central actin fibre density
Y27632
D
Relative Paracellular flux
shCtrl
shArpin
Y27632
E
shCtrl + vehicle
shCtrl + HS38
shArpin + vehicle
shArpin + HS38
Phalloidin / VE-Cadherin
F
Pixel Media Intensity (Phalloidin)
Vehicle
HS38
G
Central actin fibre density
Vehicle
HS38
H
Relative Paracellular flux
Vechicle
HS38
I
Relative Paracellular flux
shCtrl
shArpin
TNFα
Vehicle
HS38

Figure 8

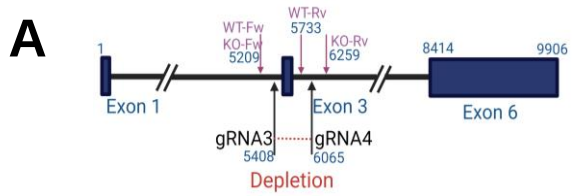
A
WT-Fw
KO-Fw
5209
WT-Rv
5733
KO-Rv
6259
1
8414
9906
Exon 1
Exon 3
Exon 6
gRNA3
5408
gRNA4
6065
Depletion

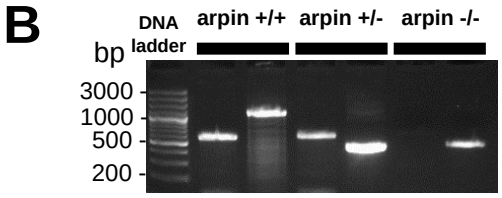
B
DNA ladder
arpin +/+
arpin +/-
arpin -/-
bp
3000
1000
500
200

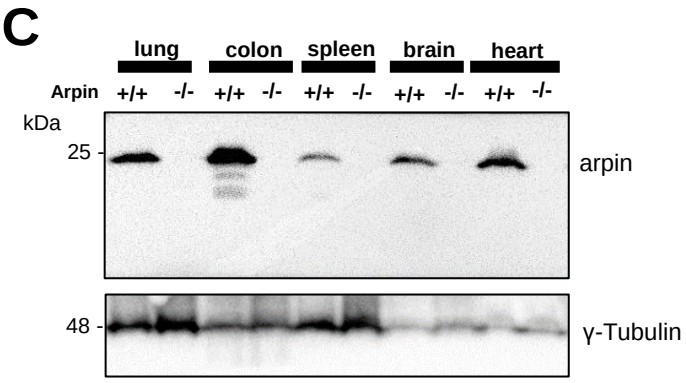
C
lung
colon
spleen
brain
heart
Arpin
+/+
-/-
kDa
25
48
arpin
γ-Tubulin

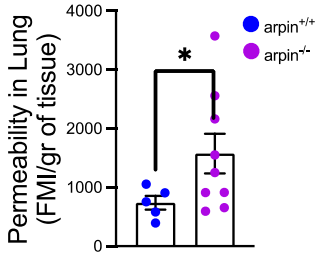
D
Permeability in Lung (FMI/gr of tissue)
4000
3000
2000
1000
0
*
arpin+/+
arpin-/-

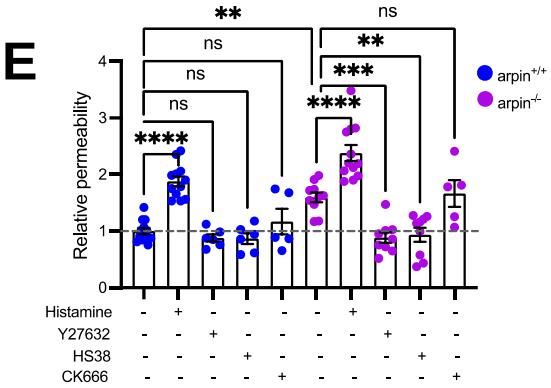
E
Relative permeability
**
ns
ns
ns
**
***
****
****
arpin+/+
arpin-/-
Histamine
Y27632
HS38
CK666

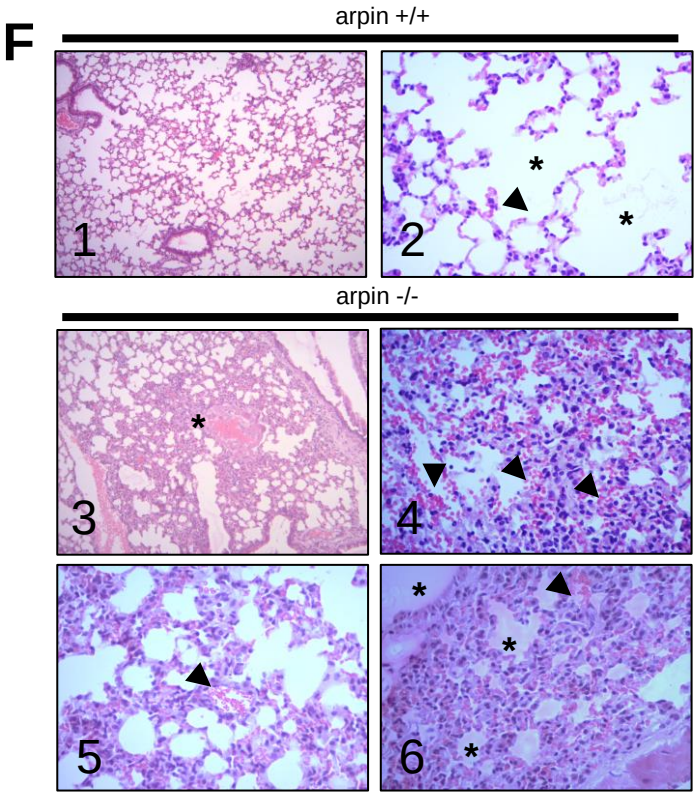
F
arpin +/+
arpin -/-
1
2
3
4
5
6

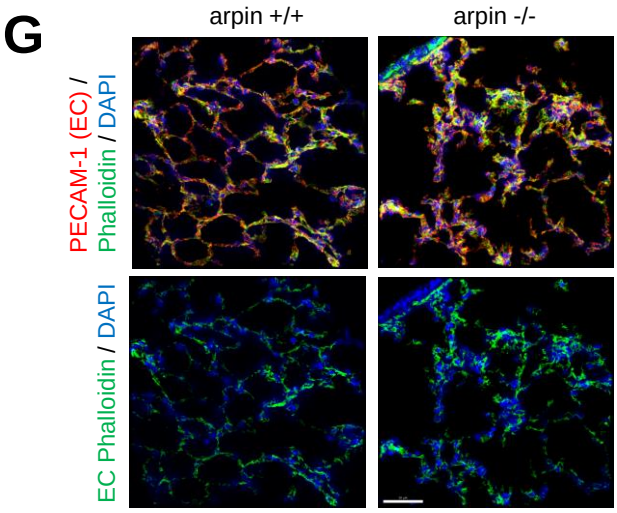
G
arpin +/+
arpin -/-
PECAM-1 (EC) / Phalloidin / DAPI
EC Phalloidin / DAPI

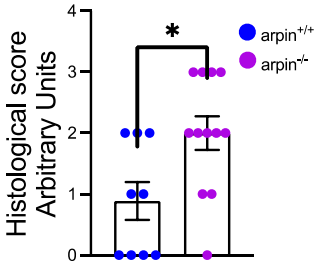
Histological score Arbitrary Units
4
3
2
1
0
*
arpin+/+
arpin-/-

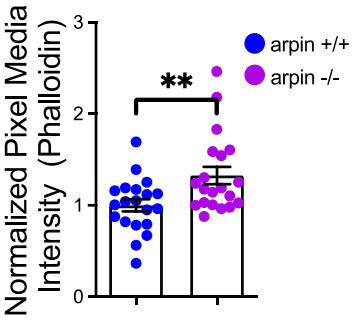
Normalized Pixel Media Intensity (Phalloidin)
3
2
1
0
**
arpin +/+
arpin -/-

Figure 9

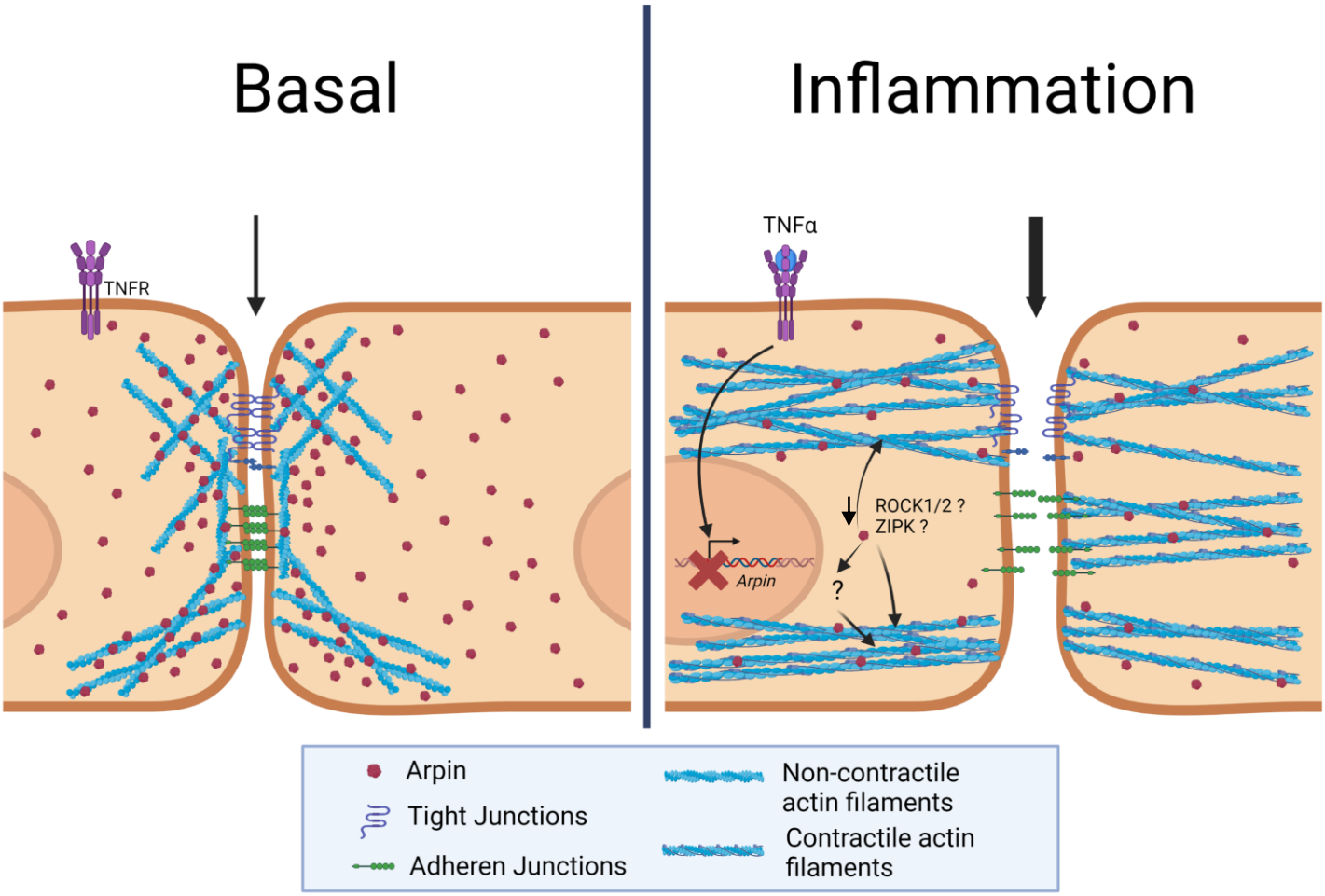
Basal
Inflammation
TNFR
TNFα
ROCK1/2 ?
ZIPK ?
Arpin
?
Arpin
Tight Junctions
Adheren Junctions
Non-contractile actin filaments
Contractile actin filaments